TAMPERE UNIVERSITY OF TECHNOLOGY

ADNAN QAMAR KIAYANI

DSP BASED TRANSMITTER I/Q IMBALANCE CALIBRATION-IMPLEMENTATION AND PERFORMANCE MEASUREMENTS

MASTER OF SCIENCE THESIS

Examiners: Professor Mikko Valkama
MSc. Lauri Anttila

Examiners and topic approved in the Computing and Electrical Engineering Faculty Council meeting on 4th March, 2009

Abstract

TAMPERE UNIVERSITY OF TECHNOLOGY

Master's Degree Program in Radio Frequency Electronics

Kiayani, Adnan Qamar: DSP Based Transmitter I/Q Imbalance Calibration-Implementation and Performance Measurements.

Master of Science Thesis, 80 Pages

October 2009

Examiners: Prof. Mikko Valkama and MSc. Lauri Anttila

Funding: Finnish Funding Agency for Technology and Innovation (TekeS), Academy of Finland, Technology Industries of Finland Centennial Foundation

Keywords: Digital compensation, direct conversion radio, I/Q imbalance, image rejection ratio, I/Q modulation, low-IF radio.

The recent interest in I/Q signal processing based transceivers has resulted in a new domain of research in flexible, low-power, and low-cost radio architectures. The main advantage of complex or I/Q up- and downconversion is that it does not produce any image signal and eliminates the need of expensive RF filters. This greatly simplifies the transceiver front-end and permits single-chip radio transceiver solutions. The analog quadrature modulators and demodulators are, however, sensitive to two kinds of implementation impairments: gain imbalance, and phase imbalance. These impairments originate due to the non-ideal behavior of the electronic components in the I- and Q-channels of the modulators/demodulators. As a result, they compromise the infinite image signal attenuation and adversely affect the performance of a wireless system. Furthermore, new higher order modulated waveforms and wideband signals are especially susceptible to these impairments and achieving sufficient image signal attenuation is a fundamental requirement for future wireless systems. Therefore, digital techniques which enhance the dynamic range of front-end with minimum amount of

additional analog hardware are becoming more popular, being also motivated by the constantly increasing number crunching power of digital circuitry.

In this thesis, some recently developed algorithms for I/Q imbalance estimation and compensation are studied on the transmitter side. The calibration algorithms use a baseband test signal combined with a feedback loop from I/Q modulator output back to transmitter digital parts to efficiently estimate the modulator I/Q mismatch. In the feedback loop, the RF signal is demodulated and compared with the original test signal to estimate the I/Q imbalance and the needed pre-distortion parameters. The actual digital transmit signal is then properly pre-distorted with the obtained I/Q imbalance knowledge, in order to cancel the effects of modulator I/Q imbalance at the data transmission phase. The performance of the compensation algorithms is first evaluated with computer simulations. A prototype system using laboratory instruments is also developed to illustrate the effects of I/Q imbalance in direct conversion and low-IF transmitters and is used to prove the usability of algorithms in real life front-ends. The results of computer simulations and laboratory measurements prove that the compensation algorithms yield a good calibration performance by suppressing the image signal interference close to or even below the noise floor.

Preface

The research work reported in this thesis has been carried out during the years 2008-2009 at the Department of Communications Engineering, Tampere University of Technology, Finland. The work has been supported by the Finnish Funding Agency for Technology and Innovation (Tekes), under the project "Advanced Techniques for RF Impairment Mitigation in Future Wireless Radio Systems", and the Academy of Finland and the Technology Industries of Finland Centennial Foundation, under the project "Understanding and Mitigation of Analog RF Impairments in Multiantenna Transmission Systems", all of which are gratefully acknowledged.

I would like to extend my profound gratitude to my supervisors Prof. Mikko Valkama and MSc. Lauri Anttila for their guidance, support, advices, and patience during my thesis work. I also want to thank Prof. Mikko Valkama for giving me the opportunity to participate in his research group and to MSc. Lauri Anttila for his infinite tolerance with the incomplete drafts. In addition, I am deeply thankful to all the people in the department for creating a pleasant working environment, especially to the head of department, Prof. Markku Renfors. I am also Indebted to COMSATS Institute of IT, Pakistan and Higher Education Commission, Pakistan for providing me the wonderful opportunity to study in Finland and for their financial support.

Special thanks to all my friends in Finland and back at home for their moral support and care. Special thanks to Haider Ali, Usman Sheikh, Faraz Amjad, and Adeel Asif. Lastly, I wish to express my deepest thanks to my family for their love, and encouragement during my studies.

Tampere, October 2009.

Adnan Kiayani

Table of Contents

List of Acronyms

ADC	Analog-to-Digital Converter
AM	Amplitude Modulation
BPF	Bandpass Filter
DA	Data Aided
DAC	Digital-to-Analog Converter
DSP	Digital Signal Processing
EVM	Error Vector Magnitude
FE	Front-End
GPIB	General Purpose Interface Bus
I	In-phase
IF	Intermediate Frequency
I/Q	In-phase/Quadrature
IR	Image Reject
IRR	Image Rejection Ratio
ISI	Inter-Symbol Interference
LNA	Low Noise Amplifier
LO	Local Oscillator
LP	Low Pass
LS	Least Squares
ML	Maximum Likelihood
NDA	Non-Data Aided
OFDM	Orthogonal Frequency Division Multiplexing
PA	Power Amplifier

PCB	Printed Circuit Board
PM	Phase Modulation
Q	Quadrature
QAM	Quadrature Amplitude Modulation
RF	Radio Frequency
R&S	Rohde & Schwarz
SAW	Surface Acoustic Wave
SNR	Signal-to-Noise Ratio
WL	Widely-Linear
WLLS	Widely-Linear Least-Squares

List of Symbols

$F\{.\}$	Fourier transform
f	frequency
f_C	carrier frequency or LO frequency
f_{IF}	intermediate frequency
g_T	amplitude/gain imbalance of transmitter LO
g_{fb}	gain of feedback loop
$g_{1,T}(t); g_{2,T}(t)$	impulse responses of the transmitter I/Q imbalance filters
$\tilde{g}_{1,T}(t), \tilde{g}_{2,T}(t)$	impulse responses of the observable I/Q imbalance filters
$\mathbf{g}_{1,T}, \mathbf{g}_{2,T}$	impulse response vectors of the transmitter I/Q imbalance filters
$\tilde{\mathbf{g}}^{0}_{2,T}$	zero padded version of $\tilde{\mathrm{g}}_{2,\mathrm{T}}$
$g_I(t); g_Q(t)$	impulse response of I- and Q- braches of the channel
$g_{ij}(t)$	real filters impulse responses modeling the transmitter I/Q imbalance
$g_D(t)$	impulse response of the direct signal
$g_M(t)$	impulse response of the image signal
$G_{i,T}(z)$	transfer function of $\mathbf{g}_{i,T}$
$G_{i,T}(f)$	frequency response of $g_{i,T}(t)$
$\mathrm{g_I}; \mathrm{g_Q}$	I- and Q- channel impulse response vectors
$\hat{\mathrm{g}}_{\mathrm{I}}; \hat{\mathrm{g}}_{\mathrm{Q}}$	least-squares estimate of $\mathrm{g_I}; \mathrm{g_Q}$
$G_I(z); G_Q(z)$	transfer function of $\mathrm{g_I}; \mathrm{g_Q}$
$h_T(t)$	impulse response of relative non-ideal transfer function between I- and Q- branches
$h_{fb}(t)$	feedback channel impulse response
i	index

$\mathbf{I}$	identity matrix
$\mathrm{Im}[.]$	imaginary part of complex signal
$IRR(f)$	frequency dependent image rejection ratio without pre-distortion
$IRR_{PD}(f)$	frequency dependent image rejection ratio after pre-distortion
$J(.)$	cost function for optimum channel coefficients
L_b	length of observed data block
N_g	length of imbalanced filter vector
N_w	length of pre-distortion filter vector
$\mathrm{Re}[.]$	real part of complex signal
$s(t)$	modulator output signal
$\mathbf{s}$	modulator output signal vector
t	time
$\mathbf{w}$	pre-distortion filter coefficients vector
$w_{ij}(t)$	real pre-distortion filters
$w_D(t)$	impulse response of pre-distortion filter for direct signal
$w_M(t)$	impulse response of pre-distortion filter for mirror signal
$x(t)$	baseband signal
$x_P(t)$	pre-distorted baseband signal
$\mathbf{x}$	baseband data vector
$y(t)$	feedback signal
$z(t)$	baseband equivalent of RF signal
$z_P(t)$	pre-distorted baseband equivalent of RF signal
$\mathbf{0}$	vector containing zeros only
$\mathbf{1}$	vector containing ones only
φ_T	phase imbalance of transmitter LO
$\delta(t)$	dirac delta function
σ^2	variance of a quantity

$(.)_{OPT}$	optimum value of a quantity
$(.)_P$	pre-distorted signal
$(.)^T$	transpose of a matrix or vector
$(.)^{-1}$	inverse of a matrix
$(.)^*$	complex conjugate of a quantity
$(.)^H$	Hermitian transpose of a matrix
$(.)^+$	pseudo-inverse of a matrix
$\|\|.\|\|$	norm of a vector

Chapter 1

Introduction

1.1 Motivation and Background

For the past several years, wireless communication sector has experienced unprecedented growth with new standards emerging offering improved quality of service to the users. According to the GSM Association (GSMA) [53], there are currently more than 3 billion cellular users worldwide and this number is expected to grow exponentially. The rapid growth of cellular users indicates a bright future for wireless communication industry and also offers plenty of room for innovative research in the field.

The proliferation of various wireless standards pushes for multistandard terminals that support existing as well as emerging air interfaces. One approach of designing a multistandard/multimode transceiver is to build a flexible system that can be programmed to operate at all communication modes [10], [11], [13]. However, the design of such a device poses many technical challenges which need to be addressed to enable its operation. The growing number of wireless connections calls for higher capacity. This, combined with the advent of new emerging applications demanding much higher bandwidth per user, suggests that fundamental changes are required in radio transceiver design. In addition to that, future wireless systems will employ higher order constellations, non-constant envelope modulation schemes, and higher bandwidths to meet the user's demands of the data rates, thus making the system more susceptible to analog front-end non-idealities [10], [11]. Another bottleneck towards the evolution of wireless networks is the integration of analog and digital components of front-end on a single chip [19], [20], [34]. Fortunately, present CMOS technology offers

a high level of integration at low cost and is particularly suitable for future integrated wireless transceivers. Portability, power consumption, and cost are also important design consideration for the development of integrated transceivers.

The ambitious goal of building a single chip, fully integrated radio transceiver which covers multiple RF standards with low power consumption at a low cost has triggered new research in the field of radio architectures [2], [4], [10], [33], [36], [37]. Traditional communication transceivers are based on the superheterodyne [2], [19], [34] principle which is implemented in two stages with amplifier, radio frequency (RF), image rejection (IR), and intermediate frequency (IF) filter, mixers, and frequency synthesizers. In the first stage, on the transmitter side, the signal is shifted from baseband up to the IF frequency, second stage mixes the signal up to desired RF frequency. The effective performance of superheterodyne transmitters is delivered at the expense of increased complexity, cost, component count, current consumption, and physical size of the transmitter. Also, many connections to external lumped components restrict the single chip integration. Due to these unavoidable problems, superheterodyne architecture is impractical for integrated modern multistandard communication systems. Zero-IF or homodyne or direct conversion transmitter [2], [19], [34], [35] up-converts the signal directly from baseband to RF using a single mixing stage and eliminates the need of image rejection filters, which yields easy integration of front-end components. However, there are also some problems associated with this architecture which include local oscillator (LO) signal leakage, I/Q imbalance, 1/f noise, and inter-modulation distortion. These nonlinearities reduce the dynamic range significantly. Low-IF [19], [21], [34] transmitter up-converts the channel signals located at a low intermediate (IF) frequency to desired RF frequency.

Zero-IF and low-IF approaches offer a high level of integration and promise multistandard operation. Both architectures are based on the I/Q mixing principle which in theory provides infinite attenuation of image signal, thus relaxing RF filtering requirements [20], [23], [24]. However, the differences between the analog components on the I- and Q- branches of the modulator result in only a finite attenuation of image frequencies. This problem is known as I/Q imbalance and it causes crosstalk between the wanted and image channel signals, thereby reducing the signal to interference ratio.

1.2 Scope and Outline of the Thesis

One fascinating approach towards constructing a flexible wireless communication system at a reduced cost is to study the impact of analog non-idealities on the used waveforms and to develop digital compensation techniques for their calibration. The *Dirty RF* [32] paradigm suggests tolerating the RF impairments to a certain degree and compensating them in digital domain. The common non-idealities in a radio transceiver include I/Q problem, oscillator phase noise, power amplifier non-linearity, timing jitter and other non-idealities of analog-to-digital converters (ADC) [10], [11]. By compensating these non-idealities digitally, the specifications of individual analog modules can be relaxed and the cost of overall front-end can be reduced significantly.

In this thesis, the feasibility of digital signal processing based I/Q imbalance mitigation techniques is evaluated on the transmitter side. This thesis is organized in six chapters. In Chapter 2, basic concepts related to I/Q mixing are introduced followed by a review of transmitter architectures including typical superheterodyne, direct conversion, and low-IF architectures. Also, most important impairments arising in the components of transmitters are discussed shortly at the end of the chapter. Chapter 3 starts with the analytic description of I/Q imbalance and mathematical modeling of transmitters' I/Q mismatch is presented. The impact of I/Q imbalance in direct conversion and low-IF is discussed based on the developed mathematical model and afterwards, digital pre-distortion based I/Q imbalance compensation algorithms are reviewed. Chapter 4 reports the computer simulation results of the compensation algorithms with various signal types. The aim of is to demonstrate the development of the measurement setup. The measurement setup is based on the generic compensator structure introduced in Chapter 3 and models a real world transmitter front-end. It allows assessing the performance of calibration algorithms. Measurement results for different signal models are delineated in the chapter. Finally, Chapter 6 draws the conclusion of the thesis.

Chapter 2

Fundamentals of Radio Transmitter Architectures

Future wireless systems are required to support higher data rates to a large number of coexisting users, using a wide variety of different applications and different existing and evolving wireless systems. The objective of building a radio system that allows a great deal of flexibility, but is still affordable and portable calls for highly integrable transceivers [10], [11], [32], [40], [42]. Current radio transceivers employ digital signal processing (DSP) techniques to meet these demands. Many of the functionalities of a transceiver which have traditionally been implemented with analog radio frequency (RF) circuits are now taken over by digital signal processors. In the literature, different transceiver architectures have been proposed each with their corresponding advantages and disadvantages. The objective of this chapter is to give a brief introduction to the traditional and modern transceiver architectures and to discuss the imperfections and impairments that take place in their constituent blocks. Since the thesis is focusing on the transmitter side, only transmitter architectures are considered.

The chapter starts with the representation of signals in time and frequency domain and introduces real and complex-valued signals. In order to establish the basis for the transmitter's architecture, mixing techniques are then discussed in section 2.3. Transmitter architectures based on real and complex mixing are addressed in Section 2.4. Finally, an overview of the fundamental RF impairments often encountered in wireless transceivers is presented.

2.1 Real and Complex-Valued Signals

The target of a telecommunication system is to transport the information from one place to another. This information is represented with signals which may be in the form of voltage, current, or electromagnetic wave. Any information bearing signal can be described in the time domain and/or in the frequency domain and there exists a relationship between these descriptions [15], [16], [18]. A time domain signal is often called a continuous time signal and is a function of time t. If this time domain signal $x(t)$ has finite energy then it can be equivalently represented in the frequency domain $X(f)$ by taking its Fourier transform. The Fourier transform describes which frequencies are present in the signal and the frequency domain signal is viewed as consisting of sinusoidal components at various frequencies. The mathematical expression of a Fourier transformed signal is given in the following equation

$$X(f) = F\{x(t)\} = \int_{-\infty}^{\infty} x(t)e^{-j2\pi ft}dt \tag{2.1}$$

The magnitude of above signal $\left|X(f)\right|$ when plotted as a function of frequency f is known as the amplitude spectrum of the signal. The corresponding inverse Fourier transform is

$$x(t) = F^{-1}\{X(f)\} = \int_{-\infty}^{\infty} X(f)e^{j2\pi ft}df \tag{2.2}$$

A Fourier transform pair is formally denoted by $x(t) \xleftrightarrow{F} X(f)$. Physical signals, such as voltage or current over time, are real-valued and the Fourier transform of a real-valued signal obeys the Hermitian symmetry i.e. $X(-f) = X^*(f)$, where $(.)^*$ denotes complex conjugation [15], [16]. The amplitude spectrum of a real-valued baseband signal is depicted in Figure 2.1-a, which shows the spectral symmetry of real-valued signals. Complex-valued or in-phase quadrature (I/Q) signals are often utilized in radio signal processing. A complex-valued signal is a pair of two real-valued signals, consisting of a *real* and an *imaginary* component. Mathematically, a complex-valued signal is written as

$$x(t) = x_I(t) + jx_Q(t) \tag{2.3}$$

The real part of the signal $x_I(t)$ is known as in-phase signal and the imaginary part $x_Q(t)$ is known as quadrature signal. The spectrum of a complex-valued baseband signal does not need to obey any symmetry, as shown in Figure 2.1-b.

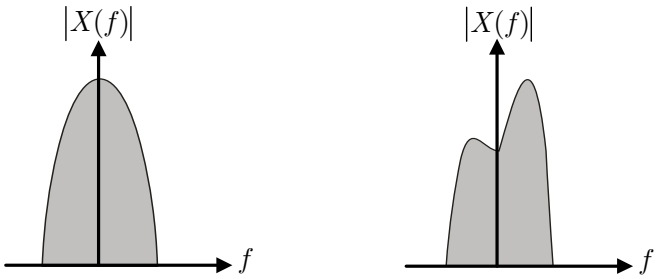

(a) *(b)*

***Figure 2.1**: Amplitude spectrum (a) real-valued baseband signal (b) complex-valued baseband signal.*

2.2 Bandpass Transmission

In the context of wireless communications, a signal whose spectral magnitude is nonzero for frequencies in the vicinity of the origin (i.e. $f = 0$) is often referred to as baseband or lowpass signal [15], [18]. On the other hand, a signal which has a spectrum concentrated about a carrier frequency $f = \pm f_C$, where f_C denotes the carrier frequency, is called bandpass signal. Modulating a complex exponential $e^{j2\pi f_C t}$ by a complex-valued baseband signal $x(t) = x_I(t) + jx_Q(t)$ yields a complex-valued analytic signal [18] which consists of only positive frequency components. Mathematically, this can be described as a Fourier transform pair as

$$x(t)e^{j2\pi f_C t} \xleftrightarrow{F} X(f - f_C) \tag{2.4}$$

The physical medium of transmission in telecommunication is real-valued and a complex-valued signal cannot be transmitted over the real-valued channel. However, using the lowpass-to-bandpass transformation, a complex-valued low pass signal can be transmitted over a real-valued bandpass channel [15], [20]. The corresponding real-valued bandpass signal for the above given modulated signal can be defined as

$$s(t) = 2\,\mathrm{Re}\left\{x(t)e^{j2\pi f_C t}\right\} = x(t)e^{j2\pi f_C t} + x^*(t)e^{-j2\pi f_C t} \tag{2.5}$$

An equivalent representation of (2.5), called quadrature carrier form, is

$$s(t) = 2x_I(t)\cos(2\pi f_C t) - 2x_Q(t)\sin(2\pi f_C t) \tag{2.6}$$

The corresponding frequency domain representation is

$$S(f) = X(f - f_C) + X^*(-f - f_C) \tag{2.7}$$

where $X(f) = F\{x(t)\} = F\{x_I(t) + jx_Q(t)\}$. The spectrum of above bandpass signal constitutes the positive and negative frequency components and it is symmetric about the zero frequency, though non-symmetric about the carrier frequency. A bandpass transmission system based on (2.6) is shown in Figure 2.2.

Similar to lowpass-to-bandpass transformation, any real-valued bandpass signal can be represented as a complex-valued lowpass or baseband signal, known as equivalent baseband signal, using bandpass-to-lowpass transformation [18]. The equivalent baseband signal can be written as

$$x(t) = LP\{s(t)e^{-j2\pi f_C t}\} \tag{2.8}$$

where LP denotes lowpass filtering.

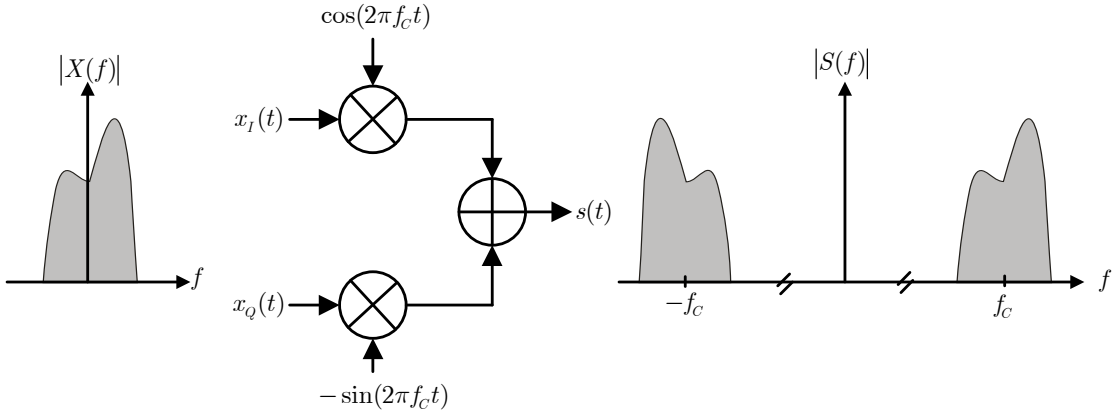

Figure 2.2: *Bandpass transmission system.*

2.3 Mixing Techniques

A physical transmission medium is typically incapable of transmitting frequencies at d.c. and near d.c. So, it is required to translate the baseband signal to a frequency range that is suitable for the communication channel. This frequency translation is carried out by mixing the baseband signal with the local oscillator signal. There are two approaches to perform the mixing operation- real mixing and complex mixing. These two techniques are discussed in the following subsections.

2.3.1. Real Mixing

Real mixing is based on multiplying a real-valued signal with a real-valued sinusoid. The sinusoidal signal is generated by a local oscillator and the resulting output signal has a spectrum similar to the original signal, but translated up and down by f_C, where f_C is the frequency of the local oscillator [15], [16], [19], [36]. The real mixing process can be described with the following equation

$$s(t) = x(t)\cos(2\pi f_C t) = x(t)\frac{1}{2}(e^{j2\pi f_C t} + e^{-j2\pi f_C t}) \tag{2.9}$$

The Fourier transform of the above equation yields the frequency domain result as

$$S(f) = \frac{1}{2}X(f - f_C) + \frac{1}{2}X(f + f_C) \tag{2.10}$$

Figure 2.3 shows a bandpass signal generated by real mixing a desired channel signal located originally at an intermediate frequency f_{IF}. The output signal spectrum consists of sum of the two copies of original input signal.

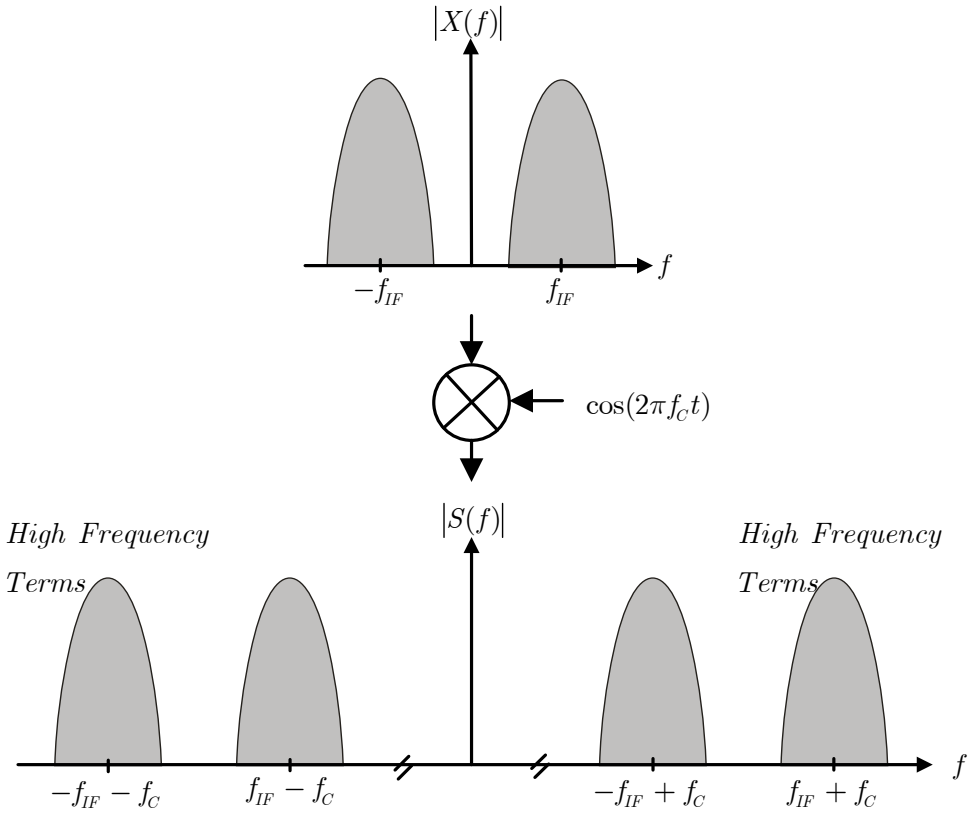

Figure 2.3: *A frequency domain illustration of mixing a real-valued signal with a real-valued sinusoid.*

The situation is more problematic when a modulated bandpass signal is real-mixed with an oscillator signal for downconversion. Due to two frequency translations, the frequency band at and around $-f_C$ is superimposed upon the frequency band at and around f_C. The undesired band is called the image signal and this problem is known as image signal problem and depicted in Figure 2.4. This problem can be prevented with the use of an image reject (IR) filter, which suppresses the image signals prior to mixing [2], [19], [34]. In the case when local oscillator frequency is equal to the centre frequency of the signal, the image band appears on top of the desired signal and it cannot be avoided with the IR filter. Also, some higher frequency terms are produced during the mixing operation and they are filtered out by the lowpass filter.

Real mixing technique is successfully deployed in the traditional super-heterodyne architectures. An image rejection filter located after the mixing stage is used to attenuate the image band signals.

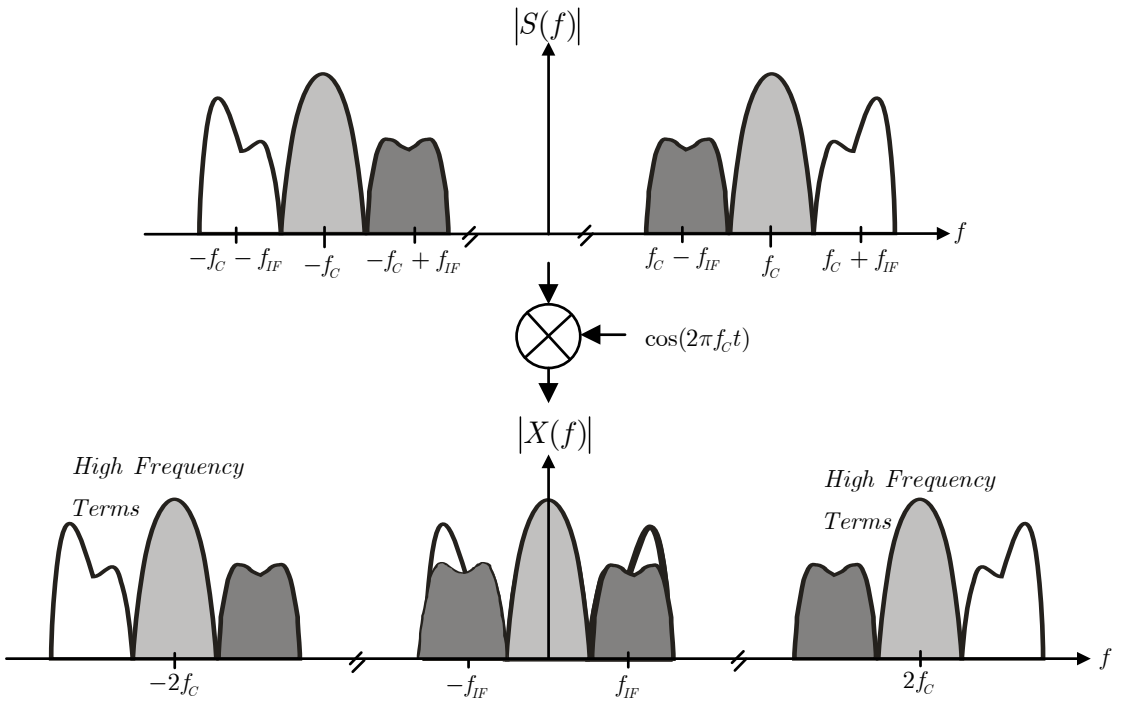

Figure 2.4: *A frequency domain illustration of down-converting a real-valued bandpass signal using real mixing technique. A specific channel signal and its image are separated by 2 f_{IF}. The spectrum of down-converted signal is represented without image rejection filtering.*

2.3.2. Complex Mixing

Complex mixing approach uses a complex-valued sinusoid of frequency f_C and multiplies it with a real-valued or complex-valued input signal to obtain a bandpass signal. Compared to the traditional real mixing technique, complex mixing results in a single frequency shift, thus eliminating the image signal problem in the down-conversion [14], [19], [20]. Using phasor notation, a complex-valued LO signal can be represented as a pair of orthogonal real-valued signals as

$$e^{j2\pi f_C t} = \cos(2\pi f_C t) + j\sin(2\pi f_C t) \tag{2.11}$$

The spectrum of above mentioned complex exponential has only a single positive frequency component and mixing a real valued signal with this exponential produces a complex-valued signal whose spectrum is a shifted version of the original signal. Figure 2.5 depicts the practical realization of complex mixing in the case of complex-valued input signal. The in-phase and quadrature components of the input signal are

modulated by the real and imaginary parts of LO signal. As shown, the mixer uses four real multiplications and two real additions. However, as said earlier that only real part is transmitted on the channel and it contains all the information about the signal. Thus, the structure of Figure 2.5 simplifies to the one shown in Figure 2.2. The output complex-valued bandpass signal has following form

$$s(t) = x(t)e^{j2\pi f_C t} \tag{2.12}$$

And the equivalent Fourier transform is

$$S(f) = X(f - f_C) \tag{2.13}$$

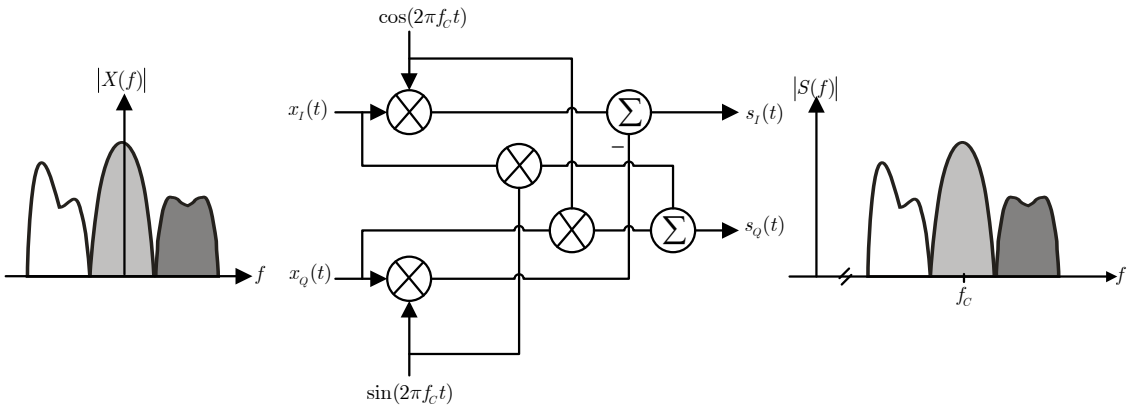

Figure 2.5: *An illustration of complex mixing process for a complex-valued input signal. Practical realization of complex mixing process requires four real multiplications and two summations. A frequency domain illustration shows that complex mixing results in a single frequency shift. Here, ideal matching of the I- and Q-branches is assumed.*

A practical implementation challenge of complex mixing is the perfect matching in magnitude and phase of the I- and Q-branches, which provides infinite image attenuation. In practice it is not possible to satisfy this requirement and there is always some amplitude and phase imbalance between the quadrature channels which leads to only finite image signal attenuation. This problem is known as I/Q imbalance and will be discussed in more detail in Chapter 3.

This type of mixing approach can be found in direct conversion radio transceivers as well as low-IF transceivers. The advantage of providing infinite image rejection

eliminates the need for image rejection filter in the transceivers front-end and simplifies the overall architecture.

2.4 Review of Transmitter Architectures

An RF transmitter performs three essential tasks- modulation, upconversion, and power amplification. Early radio transmitters are based on the conventional heterodyne architecture. These radio transmitters provide good performance compared with the others; however, they suffer from high production cost, high power consumption, and the difficulty to integrate the radio frequency (RF) and intermediate frequency (IF) filters in a single chip. Most recently, direct conversion or homodyne architecture has become quite popular due to the obtained cost saving and simple architecture, but it also has some drawbacks. A modified architecture known as low-IF architecture is able to overcome some of the problems of direct conversion architecture.

The first subsection discusses the super-heterodyne architecture and reveals its implementation challenges. The key issues related to the direct conversion architecture are described next. Finally, the low-IF architecture is examined.

2.4.1. Superheterodyne Architecture

The conventional super-heterodyne architecture [1], [2], [19], [34] is widely used in communication transceivers and measurement devices. The architecture is based on mixing the incoming signal with an offset frequency local oscillator (LO) to generate an IF signal. The IF signal is again mixed to produce an RF signal and transmitted after amplification by the power amplifier.

The block diagram of a super-heterodyne transmitter with quadrature modulator is shown in Figure 2.6. The baseband signals are, in most cases, generated by DSP. The digital baseband signals are converted to the corresponding analog signals by digital-to-analog (DAC) converters in the I- and Q- branches of the transmitter. After baseband filtering, the baseband signals $I(t)$ and $Q(t)$ are in phase-quadrature (I/Q) modulated at an IF frequency. The modulator output is sum of the I- and Q- IF signals and has the form

$$S(t) = I(t)\cos(2\pi f_{IF}t) - Q(t)\sin(2\pi f_{IF}t) \tag{2.14}$$

The IF filter then filters out LO leakages, harmonics, and any mixing products that are outside the required transmitter bandwidth. The IF filtered signal is up-converted to the RF frequency by the second LO, followed by an RF filter. The function of RF filter is to suppress all the transmission leakages, the image signals and other interferences produced during the upconversion. The power amplifier (PA) boosts the RF signal to a level that is suitable for transmission and the signal is transmitted by the antenna.

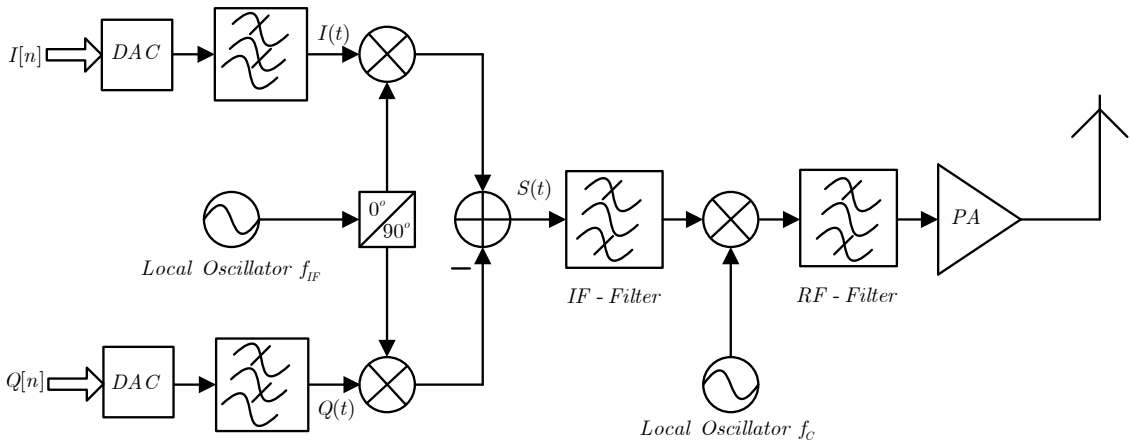

Figure 2.6: *Superheterodyne transmitter architecture.*

The high level performance of super-heterodyne transmitter is delivered at the expense of increased complexity, cost, current consumption, component count, and physical size [1], [2]. The IF and RF filters are used to attenuate transmitter's internal interferences produced due to leakages and nonlinearities. These filters increase the overall size and cost of the transmitter [14], [34]. Also, the quadrature modulation relies on equal gain and exact 90^o phase difference between the I- and the Q-branch. The gain and phase mismatch is termed as I/Q imbalance and deteriorates the performance of the transmitter.

2.4.2. Direct conversion Architecture

The direct conversion or zero-IF architecture [2], [17], [19], [34], [35] is based on the principle of directly up-converting the baseband signals to the RF frequency of transmitter. The block diagram of direct conversion transmitter is illustrated in Figure 2.7. DACs create the analog baseband signals which are subsequently filtered by the low pass filters. The low pass filters are usually called reconstruction filters, and their task is to filter out the extra high frequency images that are created by DACs. The filtered baseband signals drive the I- and Q- ports of the I/Q modulator. The local

oscillator frequency of I/Q modulator is chosen as the desired output frequency. The modulator output is of the form

$$S(t) = I(t)\cos(2\pi f_C t) - Q(t)\sin(2\pi f_C t) \tag{2.15}$$

As opposed to the super-heterodyne transmitter, the IF filer is not needed at the output of the modulator because no IF products are generated. Also, the selectivity requirements of RF filter are not as strict as in the case of superheterodyne transmitter. The elimination of IF filter result in a reduced cost and easy integration. The RF signal at the output of RF filter is then boosted in amplitude by the power amplifier and transmitted by the antenna.

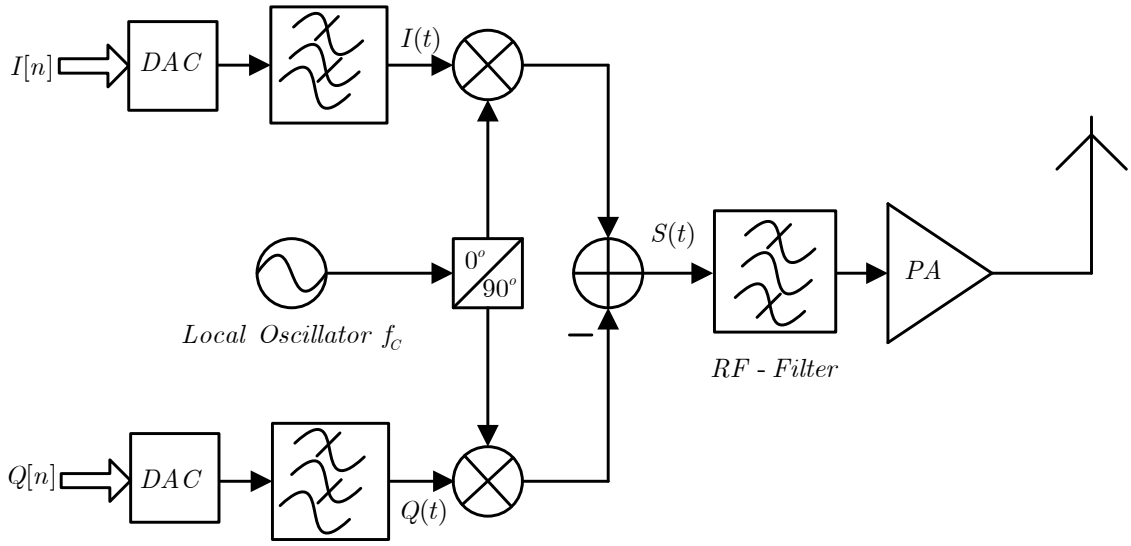

Figure 2.7: *Direct conversion transmitter architecture.*

The direct conversion architecture represents a promising solution for future wireless system due to its simple configuration but there are still number of challenges before its deployment. Some of the technical issues are shortly discussed in the following paragraphs and a more detailed description of these impairments is given in section 2.5.
The direct conversion transceivers are more susceptible to LO leakage problem than the ones based on super-heterodyne architecture [1], [2], [19]. If the baseband I- and Q-signals contain an unwanted DC component then it sums with the LO signal and is seen as a spurious tone at the LO frequency. In transmitters, LO leakage results in spurious signal energy at carrier frequency. Depending on the transmitter architecture, LO

leakage signal creates in-band interference or adjacent channel interference when received at the receiver.

LO pulling is another source of impairment in direct conversion transmitters, which occurs when some of the signal energy at the output of the PA leaks back to the LO and it causes phase modulation [1], [2], [19]. Usually, this problem appears when the PA is located close to the printed circuit board (PCB) of the transmitter and the problem can be prevented with a better layout design and effectively grounding the PCB components.

The mismatch between the amplitude of I- and Q- channel signals of the modulator and/or non-ideal quadrature splitting of the LO signal contributes to the degradation of the error vector magnitude (EVM) [1], [2], [19]. Although this problem occurs also in super-heterodyne transmitters but it's potentially more severe in direct conversion transmitters. LO frequency of I/Q modulator is not fixed in direct conversion transmitter, as in the case of super-heterodyne transmitter, which makes it difficult to achieve constant gain and exact 90^{o} phase difference at all frequencies of the modulator.

2.4.3. Low-IF Architecture

The low-IF architecture [19], [21], [34] is similar to the direct conversion architecture (Figure 2.7), except that the desired baseband signal is first translated to a frequency near zero before the DAC. Figure 2.8 shows Digital-IF transmitter architecture, where the baseband signal is up-converted to the RF frequency by a tunable digital I/Q up-converter followed by a fixed analog I/Q up-converter. The baseband signals are modulated with a complex-valued carrier resulting in an analytic bandpass signal at IF. The low-IF signal is transformed to the continuous time signal with DAC and this signal is multiplied with an analog local oscillator to produce the RF signal. The RF signal is then transmitted after amplification by the power amplifier.

For the low-IF topology, image and LO leakage signals appear on the adjacent channels after up-conversion and cause interference with the adjacent channels. This transmitter architecture is highly sensitive to the image rejection problem (or I/Q imbalance) and sufficient attenuation of image signals must be achieved prior to signal transmission.

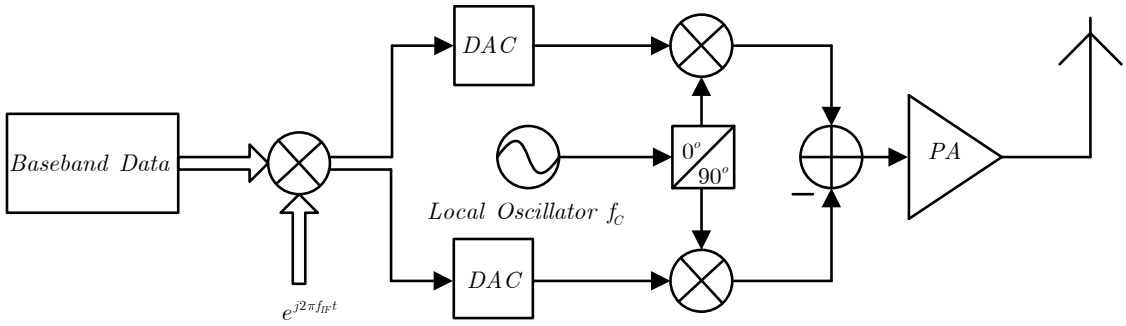

Figure 2.8: *Low-IF transmitter architecture.*

Low-IF architecture is an attractive and popular approach for receivers. It alleviates the problem of DC offset which cannot be avoided in the direct conversion receivers. It can also remove other low-frequency disturbances such as flicker noise and even-order nonlinear products. Again, these advantages are achieved at the price of increased susceptibility to the I/Q imbalance problem [17].

2.5 RF Impairments in Radio Transmitters

This section is a short introduction to the RF impairments originating in the constituent blocks of a transmitter and their impact on the performance.

2.5.1. Non-idealities of Power Amplifiers

An amplifier is an important component of any radio transmitter. It is used to amplify a signal to a level that is suitable for transmission. All RF power amplifiers exhibit some nonlinearity. Due to these nonlinearities, the signal at the output of the PA contains not only the original signal frequency contents but also some new frequency components. The effect of these new frequency components on the RF signal is two-fold: in-band distortion which results in an elevated noise floor, and out-of-band distortion which causes cross-talk and interference between different adjacent signal bands [3]-[6]. In the PA context, spreading of the transmitted signal spectrum (so-called spectral regrowth) causes out-of-band distortion which interferes with adjacent channel signals, while in-band distortion degrades the bit-error rate at the receiver.

The nonlinear distortion can be characterized as memoryless, quasi-memoryless or to contain memory, depending on the used waveform and type of power amplifier [3], [4], [8]. For narrow band input signals, the power amplifier does not typically exhibit the

memory effects and the power amplifier can be regarded as memoryless or quasi-memoryless. In the strictly memoryless case, no phase difference exists between the input and output signals, while in the quasi-memoryless case, there is a phase difference between input and output. As the bandwidth of the signal increases, the time span of the power amplifier memory becomes comparable to the time variations of the input signal level and the power amplifiers begin to show memory effects [8].

A memoryless power amplifier can be modeled by its AM-AM and a quasi-memoryless power amplifier creates AM-AM and AM-PM conversion. AM-AM is the conversion between the amplitude modulation present on the input signal(s) and the modified amplitude modulation present on the output signal [5]. A conversion from amplitude modulation on the input signal to phase modulation on the output signal is known as AM-PM conversion [5], [8], [11]. The behavior of power amplifiers with memory can be modeled with the so-called Volterra model, Wiener, Hammerstein, the Wiener-Hammerstein models, etc.

2.5.2. Non-idealities of Mixers and Local Oscillator

The function of an up-converter mixer is to translate the signal from baseband (or intermediate frequency) to RF frequency, without altering its characteristics. This is usually done by multiplying the signal with local oscillator signal which is a pure single frequency sine wave. The typical impairments introduced during the mixing operation are phase noise due to random fluctuation of the oscillator phase, LO leakage, and I/Q imbalance [10], [11], [12], [32].

In general, the local oscillator signal is not a pure sine frequency signal due to noise and other imperfections. The spectrum of such a signal is not a narrow line but appears broadened by noise. The effect of this phase noise is a phase modulation of the local oscillator signal which is transferred directly to the transmitted signal [10], [11], [12]. From the transmitted signal point of view, mixing the impaired LO signal with the ideal baseband or intermediate frequency signal produces RF signal with phase noise of LO superimposed on it. This impaired signal results in in-band as well as out-of-band distortion. A graphical illustration of phase noise phenomenon is given in Figure 2.9.

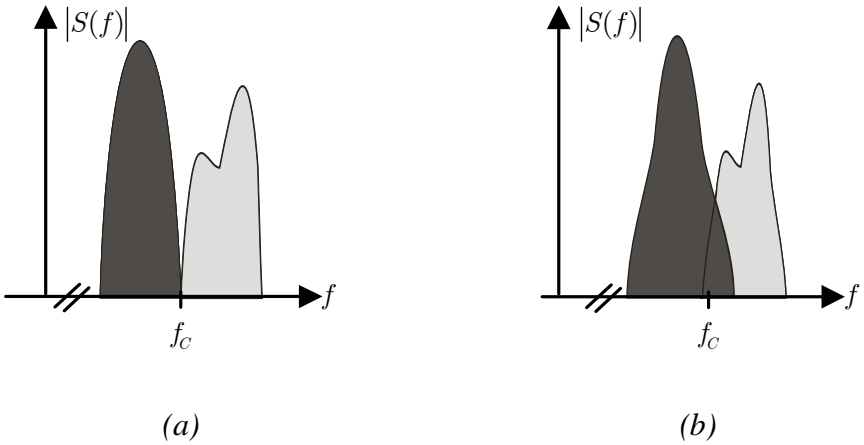

Figure 2.9: *A spectral illustration of signal distortion due to phase noise (a) original signal (b) impaired signal.*

I/Q imbalance [9], [14], [20], [23], [32] is another source of degradation related to the transmitters. Complex valued signals are often modulated by the quadrature modulators. The quadrature mixing approach theoretically provides infinite image signal attenuation. However, in practice, the mixer does not have equal gain in the I- and Q- branch, and also the phase shift between the quadrature ports is not exactly 90 degrees. In addition to that, the relative mismatch between the components in the I- and Q- branch such as LPFs and DACs contribute to the overall I/Q imbalance. These effects are called I/Q imbalance and it results in limited suppression of the image signal. For narrow band signals, the gain and phase imbalance of the mixer are typically considered as frequency independent. However, as the bandwidth of the signal gets wider the reconstruction filters and analog modulators start to exhibit frequency dependent response. The amplitude and phase mismatch causes cross talk between the mirror frequency channels. In case the modulating signal has one sided spectrum, the image signal appears on the other side of the local oscillator frequency and causes adjacent channel interference. For the case when the input signal has two sided spectrum, the image signal appear on top of the modulated signal and causes self interference. These imperfections also affect significantly the performance of power amplifier linearization circuits [24], [50]. A frequency domain illustration of the cross-talk due to I/Q imbalance in low-IF transmitter case is depicted in Figure 2.10. More details about this topic will be given in Chapter 3.

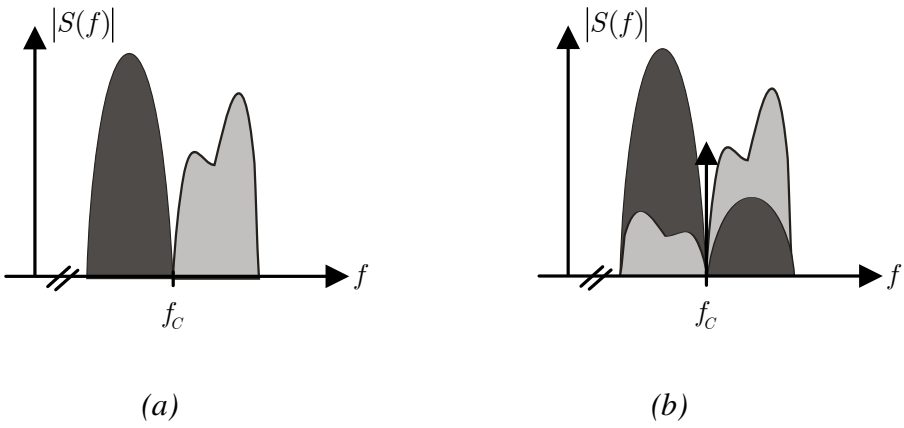

Figure 2.10: *A spectral illustration of the impact of I/Q imbalance on the modulator output (a) ideal I/Q modulator output signal assuming perfect matching between the I- and Q- branches (b) practical I/Q modulator output showing the crosstalk between the mirror channel signals.*

Another impairment is LO signal leakage through the mixer [10], [19]. LO leakage produces an undesirable spurious signal at the transmitted LO frequency. The presence of LO signal in the transmitted signal causes in-band interference for other receivers or for the intended receiver depending on the transmitter architecture.

2.5.3. Non-idealities of Digital-to-Analog Converters

Digital-to-Analog converters (DAC) are used to interface the digital part of a transmitter with its analog front-end. The non-idealities associated with DAC are quantization noise and sampling jitter [10], [11], [13]. They are described shortly in the following paragraphs.

Quantization noise [10], [11], [13] in DAC occurs due to the limited number of bits that can be used to represent a signal. A large number of bits is desirable to reduce the quantization noise, but it increases the cost and power consumption of the DAC. The quantization noise appears as an additive noise process onto the true signal and its impact can be reduced by sampling the signal at a rate much higher than the Nyquist rate.

Sampling jitter [10], [11] occurs when the instants at which DAC makes conversion of the signals are not evenly spaced. Its impact is to cause the actual sampling point to shift from its ideal position. The amount of shift is determined by the jitter. It degrades the

signal-to-noise ratio (SNR) of the signal. The greatest impact of sampling jitter is on bandpass signals because the input frequencies are very high, hence making the jitter an important parameter.

Chapter 3

Transmitter I/Q Imbalance Estimation and Compensation

Communication transceivers based on the I/Q up- and downconversion principle face a common problem of amplitude and phase mismatch [14], [20], [22], [23], [24], [38]. This problem is mainly caused by the modulators which are based on the principle of having equal gain and exact 90^{o} phase difference in the quadrature branches. However, other analog front-end components such as DACs, mixers, and filters also contribute in general to the imbalance effects [20]. Ideally, analog circuits have similar characteristics in the in-phase and quadrature branches, but in practice, due to hardware tolerances a perfectly balanced performance is not achievable. This problem leads to the finite attenuation of image signal and the degradation of signal quality. A straight forward approach to mitigate this problem is to try to improve the quality of analog modules such that the overall impact of the impairments on the system performance is at an acceptable level. Such analog solutions are presented in [28], [44]. This, however, is not feasible due to two reasons. First, the approach of designing a high quality analog module that satisfies all the transceiver specifications leads usually to a very expensive radio implementation. Second, stable performance can only be achieved over a limited frequency range which restricts the flexibility of a transceiver. A possible and attractive solution is to use digital signal processing techniques for compensating the I/Q imbalance effects [10], [11], [32], [40]. The DSP based calibration methods allow some errors in the analog design and have an advantage of achieving good performance without modifying the original transceiver architecture.

This chapter discusses the digital solutions for the calibration of I/Q imbalance problem in transmitters. In the first section of this chapter, a mathematical representation of an

imbalanced local oscillator signal is presented and a formula for image rejection ratio is derived in terms of oscillator gain and phase. The next section reviews the problem of I/Q imbalance in the context of transmitters and a frequency-dependent I/Q imbalance model is developed to show the interference of image frequency in the desired signal. Section 3.3 and 3.4 discuss the effects of I/Q imbalance in direct conversion and low-IF transmitter signals. The compensation schemes considered in [23] and [24] are summarized in section 3.5 and 3.6. The chapter concludes with the discussion of the topics studied in the chapter.

3.1 I/Q Imbalance and Image Rejection Ratio

As stated earlier that the convenient implementation of quadrature conversion suffers from the phase and amplitude imbalance in two branches, and is referred to as I/Q imbalance. The I/Q imbalance causes crosstalk between the mirror signals, and degrades the dynamic range of the transmitter and/or receiver [9], [14], [20]. The image rejection ratio (IRR) quantifies the suppression of the image signal and is defined as ratio of the desired signal power to the image signal power, and is usually expressed in dB [17], [43].

In order to derive the formula of image rejection ratio, assume that the relative gain and phase imbalance between the I- and Q- branch are given by g and φ, respectively. Then, the complex-valued LO signal can be written as

$$\begin{aligned} x_{LO}(t) &= \cos(2\pi f_C t) + jg\sin(2\pi f_C t + \varphi) \\ &= \frac{e^{j2\pi f_C t} + e^{-j2\pi f_C t}}{2} + jg\frac{e^{j(2\pi f_C t+\varphi)} + e^{-j(2\pi f_C t+\varphi)}}{2j} \\ &= e^{j2\pi f_C t}\frac{1+ge^{j\varphi}}{2} + e^{-j2\pi f_C t}\frac{1-ge^{-j\varphi}}{2} \end{aligned} \tag{3.1}$$

The above equation indicates that after modulation, the desired signal term would appear at frequency f_C with amplitude gain $\left|1+ge^{j\varphi}/2\right|$ and its undesired image will be located at $-f_C$ with amplitude gain $\left|1-ge^{-j\varphi}/2\right|$. Thus, the IRR can be expressed as

$$IRR = \frac{\left|\frac{1+ge^{j\varphi}}{2}\right|^2}{\left|\frac{1-ge^{-j\varphi}}{2}\right|^2} = \frac{1+2g\cos(\varphi)+g^2}{1-2g\cos(\varphi)+g^2} \tag{3.2}$$

With perfect I/Q balance, $g=1;\ \varphi=0$, meaning infinite image rejection ratio. For wideband signals, the imbalance parameters exhibit frequency dependent behavior and frequency-dependent IRR can be written as

$$IRR(f) = \frac{1+2g(f)\cos(\varphi(f))+g^2(f)}{1-2g(f)\cos(\varphi(f))+g^2(f)} \tag{3.3}$$

Figure 3.1 shows a plot of image rejection ratio versus the phase imbalance and amplitude imbalance. In the figure, each curve represents the image rejection ratio for a certain amplitude imbalance value. With the careful analog design, phase imbalance of 1-2^{o} and amplitude imbalance of 1-2% are achievable, resulting in 30-40dB image attenuation [29].

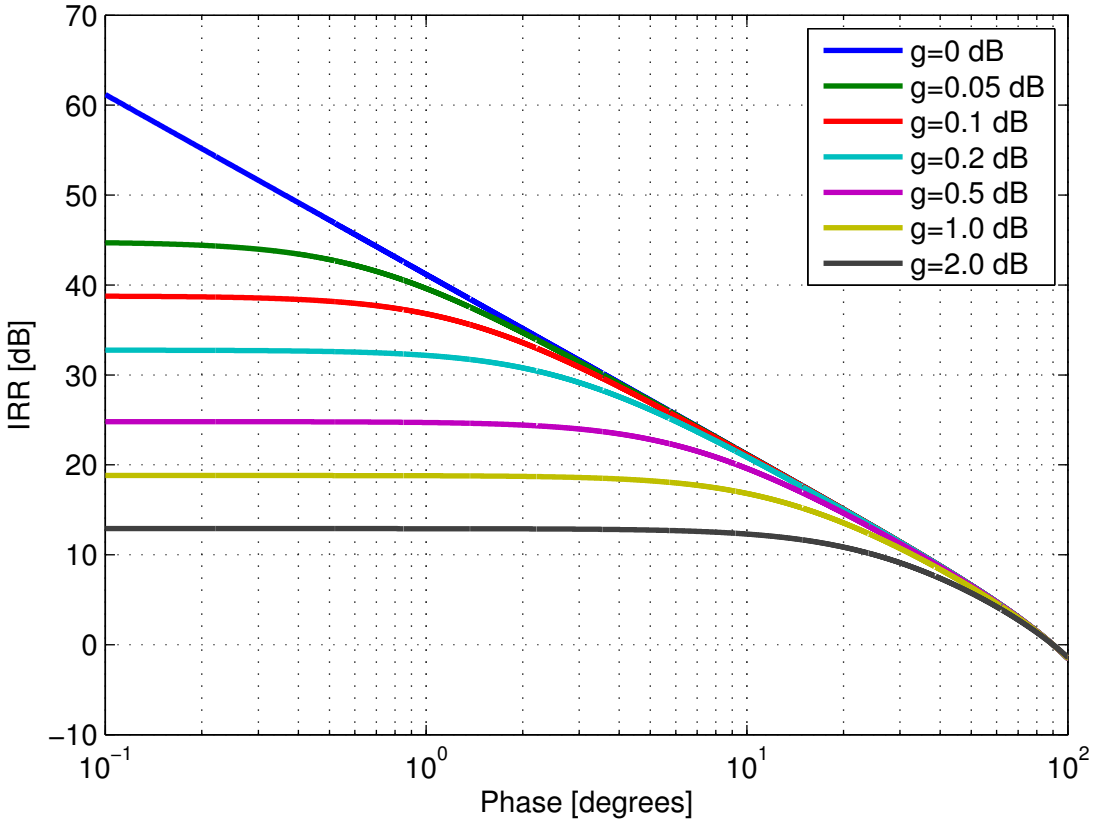

Figure 3.1: *Image rejection ratio versus gain and phase imbalance.*

3.2 Transmitter I/Q Mismatch Modeling

The recent radio transceivers such as direct conversion and low-IF utilizing the I/Q signal processing are both vulnerable to the mismatches between the in-phase and quadrature channels [38], [39]. Although they both use the quadrature mixing approach, their mirror frequency attenuation requirements are different from each other. In the following, a mathematical model is derived to illustrate the impact of I/Q imbalance in the case of direct conversion and low-IF transmitters.

3.2.1. Frequency Selective Complex I/Q Channel Model

The I/Q mismatch can be characterized by gain, phase, and frequency response mismatch between the I- and Q- branch [14], [17], [23], [24], [39]. As said earlier in the chapter that for the signals with large bandwidths, components in I- and Q- branch show frequency dependent response causing the image attenuation to vary with frequency. Figure 3.2 shows a frequency selective I/Q imbalance model in which the gain parameter g_T models the relative gain imbalance between the I- and Q- branch and the phase parameter φ_T models the relative phase difference between the quadrature channels. The relative non-ideal filter transfer function between the I- and Q- branches is modeled with the filter $h_T(t)$.

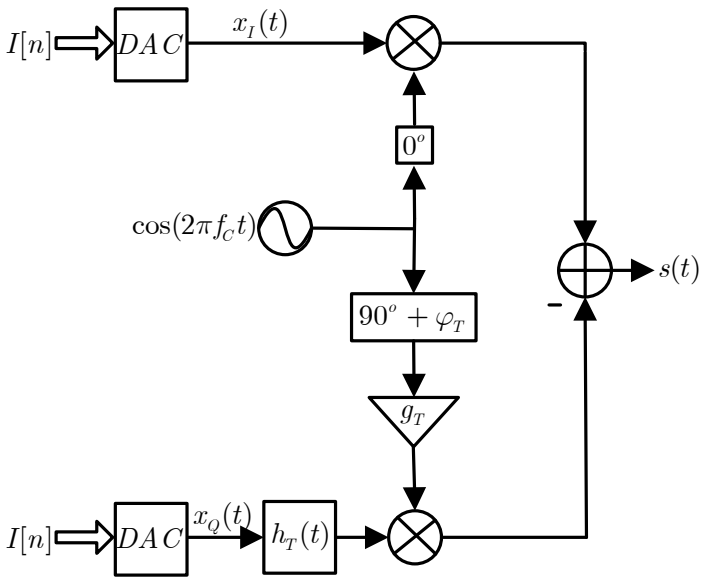

Figure 3.2: *Frequency selective I/Q imbalance model for transmitter.*

The imbalanced LO signal can be written as

$$\cos(2\pi f_C t) + j g_T \sin(2\pi f_C t + \varphi_T) \tag{3.4}$$

And the transmitted signal $s(t)$ is

$$s(t) = x_I(t)\cos(2\pi f_C t) - \big(h_T(t) * x_Q(t)\big) g_T \sin(2\pi f_C t + \varphi_T) \tag{3.5}$$

Using trigonometric identity $\sin(\alpha+\beta) = \sin\alpha\cos\beta + \cos\alpha\sin\beta$, the above equation can be composed in the form

$$\begin{aligned} s(t) = &\Big(x_I(t) - g_T \sin(\varphi_T)\big(h_T(t) * x_Q(t)\big)\Big)\cos(2\pi f_C t) - \\ &g_T \cos(\varphi_T)\big(h_T(t) * x_Q(t)\big)\sin(2\pi f_C t) \end{aligned}$$

With Euler's identity, the trigonometric functions are expressed in the complex form as

$$\begin{aligned} s(t) = &\Big(x_I(t) - g_T \sin(\varphi_T)\big(h_T(t) * x_Q(t)\big)\Big)\frac{e^{j2\pi f_C t} + e^{-j2\pi f_C t}}{2} - \\ &g_T \cos(\varphi_T)\big(h_T(t) * x_Q(t)\big)\frac{e^{j2\pi f_C t} - e^{-j2\pi f_C t}}{2j} \end{aligned}$$

Regrouping the common terms and solving them yield

$$\begin{aligned} s(t) = &\left(x_I(t) - g_T\left(h_T(t) * x_Q(t)\right)\frac{e^{j\varphi_T}}{j}\right)\frac{e^{j2\pi f_C t}}{2} + \\ &\left(x_I(t) - g_T\left(h_T(t) * x_Q(t)\right)\frac{e^{-j\varphi_T}}{j}\right)\frac{e^{-j2\pi f_C t}}{2} \end{aligned}$$

Utilizing the fact that $x(t) = x_I(t) + j x_Q(t)$, the above equation can be simplified to

$$s(t) = \left(\frac{x(t) + x^*(t)}{2} - g_T \left(h_T(t) * \frac{x(t) - x^*(t)}{2j} \right) \frac{e^{j\varphi_T}}{j} \right) \frac{e^{j2\pi f_C t}}{2} + \left(\frac{x(t) + x^*(t)}{2} - g_T \left(h_T(t) * \frac{x(t) - x^*(t)}{2j} \right) \frac{e^{-j\varphi_T}}{j} \right) \frac{e^{-j2\pi f_C t}}{2}$$

$$\begin{aligned} s(t) = & \left(g_{1,T}(t) * x(t) + g_{2,T}(t) * x^*(t) \right) e^{j2\pi f_C t} + \\ & \left(g_{1,T}(t) * x(t) + g_{2,T}(t) * x^*(t) \right)^* e^{-j2\pi f_C t} \end{aligned} \tag{3.6}$$

$$s(t) = 2\,\mathrm{Re}\left\{ (g_{1,T}(t) * x(t) + g_{2,T}(t) * x^*(t)) e^{j2\pi f_C t} \right\} \tag{3.7}$$

Here, $(.)^*$ refers to complex conjugation and $g_{1,T}(t)$ and $g_{2,T}(t)$ correspond to the imbalance filters response and are expressed in time domain form as

$$\begin{aligned} g_{1,T}(t) &\triangleq \frac{\delta(t) + g_T e^{j\varphi_T} h_T(t)}{2} \\ g_{2,T}(t) &\triangleq \frac{\delta(t) - g_T e^{j\varphi_T} h_T(t)}{2} \end{aligned} \tag{3.8}$$

The complex envelope of the transmitted RF signal $s(t)$ is

$$z(t) = g_{1,T}(t) * x(t) + g_{2,T}(t) * x^*(t) \tag{3.9}$$

In the ideal case when there is no I/Q imbalance i.e. $g_T = 1, h_T(t) = \delta(t), \varphi_T = 0$ (3.9) reduces to $z(t) = x(t)$.

The baseband model based on (3.9) is shown in Figure 3.3, where I/Q imbalance is modeled by the complex imbalance filters $g_{1,T}(t)$ and $g_{2,T}(t)$.

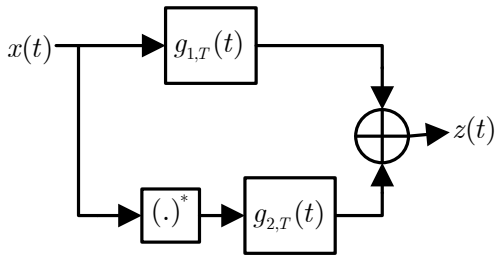

Figure 3.3: *Block diagram of the complex I/Q channel model. I/Q imbalance is modeled with complex filters.*

By using the Fourier transform, the baseband equivalent signal in (3.9) can be represented in the frequency domain as

$$Z(f) = G_{1,T}(f)X(f) + G_{2,T}(f)X^*(-f) \tag{3.10}$$

The above equation indicates that the I/Q imbalanced baseband signal is a weighted sum of the desired signal $X(f)$ and the undesirable image signal $X^*(-f)$.The weighting factor $G_{1,T}(f)$ and $G_{2,T}(f)$ are determined by the relative differences between the in-phase and quadrature branches. The undesired image signal produced due to I/Q imbalance results in the cross-talk between the mirror frequencies, as evident from (3.10)

From (3.10) the image rejection ratio (in dB) can be defined as

$$IRR(f)[dB] = 10\log_{10}\left(\frac{\left|G_{1,T}(f)\right|^2}{\left|G_{2,T}(f)\right|^2}\right) \tag{3.11}$$

3.2.2. Frequency Selective Real I/Q Channel Model

The I/Q imbalance due to frequency dependent behavior of analog components in the I- and Q- paths can be modeled with the complex filters (so-called imbalance filters) as in (3.9). These complex filters, however, can be modeled with several cross coupled real filter [24], [28]. Hence, the baseband equivalent of RF signal given in (3.9) can also be written as in (3.12) where $x(t) = x_I(t) + jx_Q(t)$ is the baseband input, and $g_{1,T}(t) = g_{1,T,I}(t) + jg_{1,T,Q}(t)$, $g_{2,T}(t) = g_{2,T,I}(t) + jg_{2,T,Q}(t)$ are the complex filters modeling the transmitter I/Q imbalance.

$$z(t) = \left(g_{1,T,I}(t) + jg_{1,T,Q}(t)\right) * \left(x_I(t) + jx_Q(t)\right) + \left(g_{2,T,I}(t) + jg_{2,T,Q}(t)\right) * \left(x_I(t) + jx_Q(t)\right)^* \tag{3.12}$$

$$z(t) = \left(g_{1,T,I}(t) + g_{2,T,I}(t)\right) * x_I(t) + \left(-g_{1,T,Q}(t) + g_{2,T,Q}(t)\right) * x_Q(t) + j\left\{\left(g_{1,T,Q}(t) + g_{2,T,Q}(t)\right) * x_I(t) + \left(g_{1,T,I}(t) - g_{2,T,I}(t)\right) * x_Q(t)\right\} \tag{3.13}$$

$$z(t) = \left\{g_{11}(t) * x_I(t) + g_{12}(t) * x_Q(t)\right\} + j\left\{g_{21}(t) * x_I(t) + g_{22}(t) * x_Q(t)\right\} \tag{3.14}$$

where

$$g_{11}(t) = g_{1,T,I}(t) + g_{2,T,I}(t);\ g_{12}(t) = -g_{1,T,Q}(t) + g_{2,T,Q}(t)$$
$$g_{21}(t) = g_{1,T,Q}(t) + g_{2,T,Q}(t);\ g_{22}(t) = g_{1,T,I}(t) - g_{2,T,I}(t)$$

A structure consisting of above given four real filters is shown in Figure 3.4, which models the I- and Q- channels and cross-coupling between them.

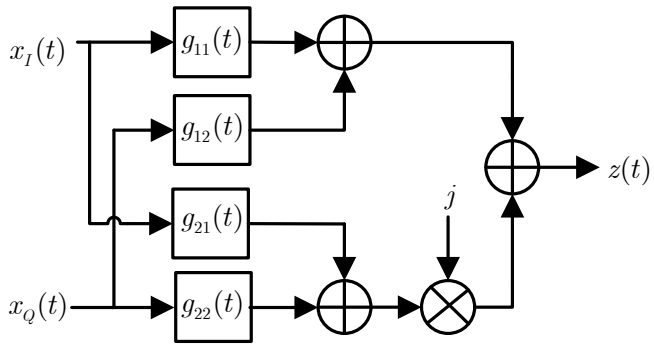

Figure 3.4: *Block Diagram of real I/Q channel model. Real filters models the I/Q imbalance.*

Combining the terms that have $x_I(t)$ or $x_Q(t)$ and rewriting (3.14) in a more compact form as

$$z(t) = x_I(t) * g_I(t) + x_Q(t) * g_Q(t) \tag{3.15}$$

where

$$g_I(t) = g_{11}(t) + jg_{21}(t);\ g_Q(t) = g_{12}(t) + jg_{22}(t)$$

It is, however, not clear from (3.15) how the modulator imbalance affects the input signal. To show the modulator nonlinearities effects, (3.15) is written as a function of the input signal $x(t)$ and its image $x^*(t)$.

$$z(t) = \left(\frac{x(t) + x^*(t)}{2}\right) * g_I(t) + \left(\frac{x(t) - x^*(t)}{2j}\right) * g_Q(t) \tag{3.16}$$

$$z(t) = x(t) * \left(\frac{g_I(t) - jg_Q(t)}{2}\right) + x^*(t) * \left(\frac{g_I(t) + jg_Q(t)}{2}\right) \tag{3.17}$$

$$z(t) = x(t) * g_D(t) + x^*(t) * g_M(t) \tag{3.18}$$

where $g_D(t)$ and $g_M(t)$ are complex filters modeling the direct and image transfer functions. The image signal appears when $g_I(t) \neq -jg_Q(t)$, i.e., $g_M(t) \neq 0$.

In the following, (3.17) is expanded to yield (3.9).

$$\begin{aligned} g_I(t) &= g_{11}(t) + jg_{21}(t) = \left(g_{1,T,I}(t) + g_{2,T,I}(t)\right) + j\left(g_{1,T,Q}(t) + g_{2,T,Q}(t)\right) \\ &= \left(g_{1,T,I}(t) + jg_{1,T,Q}(t)\right) + \left(g_{2,T,I}(t) + jg_{2,T,Q}(t)\right) = g_{1,T}(t) + g_{2,T}(t) \end{aligned} \tag{3.19}$$

$$\begin{aligned} g_Q(t) &= g_{12}(t) + jg_{22}(t) = \left(-g_{1,T,Q}(t) + g_{2,T,Q}(t)\right) + j\left(g_{1,T,I}(t) - g_{2,T,I}(t)\right) \\ &= j\left(g_{1,T,I}(t) + jg_{1,T,Q}(t)\right) - j\left(g_{2,T,I}(t) + jg_{2,T,Q}(t)\right) = j\left(g_{1,T}(t) - g_{2,T}(t)\right) \end{aligned} \tag{3.20}$$

Substituting (3.19) and (3.20) in (3.17) produces

$$\begin{aligned} z(t) = x(t) * &\left(\frac{\left(g_{1,T}(t) + g_{2,T}(t)\right) - (j)^2\left(g_{1,T}(t) - g_{2,T}(t)\right)}{2}\right) + \\ x^*(t) * &\left(\frac{\left(g_{1,T}(t) + g_{2,T}(t)\right) + (j)^2\left(g_{1,T}(t) - g_{2,T}(t)\right)}{2}\right) \end{aligned} \tag{3.21}$$

$$z(t) = g_{1,T}(t) * x(t) + g_{2,T}(t) * x^*(t) \tag{3.22}$$

Thus, the real I/Q channel is an extension of the complex I/Q channel.

From (3.18) the image rejection ratio can be defined as

$$IRR(f)[dB] = 10\log_{10}\left(\frac{|G_D(f)|^2}{|G_M(f)|^2}\right) \tag{3.23}$$

3.3 Effect of I/Q Imbalance in Direct Conversion Transmitters

In the case of direct conversion transmitters, local oscillator frequency is equal to the desired signals' centre frequency and according to (3.10), the image signal after upconversion appears on top of the desired signal. This effect is seen as a specific kind of non-linear distortion of the original signal constellation and causes self interference in the transmitted signal, as illustrated in Figure 3.5. Figure 3.6 shows the effect of gain imbalance of 20% (Figure 3.6-b), phase imbalance of 20°(Figure 3.6-c), and both gain and phase imbalance (Figure 3.6-d) on a 16-QAM modulated signal in a single channel direct conversion transmitter case. It is apparent from the figure that constellation points expand and skew due to gain and phase imbalance, respectively.

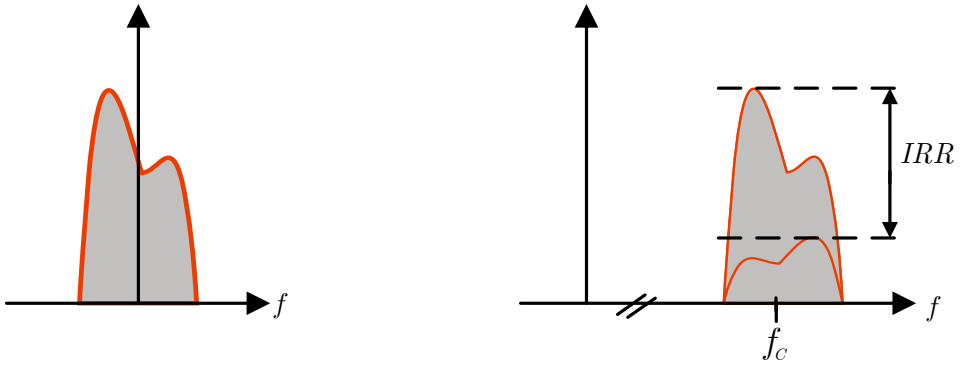

Figure 3.5: *A spectral illustration of the impact of I/Q imbalance in direct conversion transmitters (a) baseband signal (b) RF signal .*

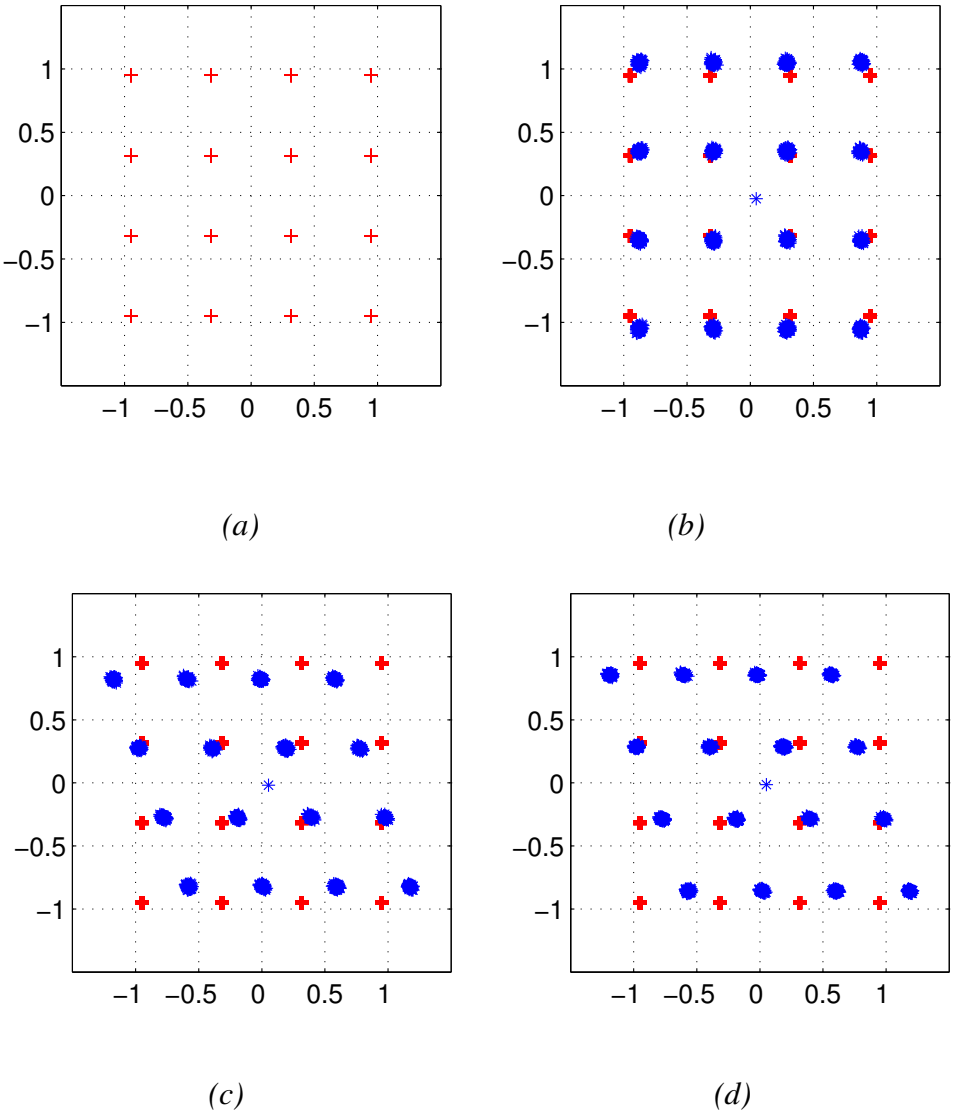

Figure 3.6: *Effect of I/Q imbalance in direct conversion transmitters (a): no I/Q imbalance (b): gain imbalance of 20% (c): phase imbalance of 20^o (d): combined effect of gain and phase imbalance.*

The image signal attenuation requirements for the direct conversion transmitters and receivers are not very strict and 20-40dB image attenuation offered by analog front-ends is likely to be enough for single carrier signals [22]. However, higher order modulation schemes, such as 64-QAM or OFDM signals, are more sensitive to gain and phase errors and a small imbalance may deteriorate the performance of the system. Also, direct conversion transmitters are more susceptible to the LO signal leakage, LO pulling and other imperfections as described in section 2.4.2.

3.4 Effect of I/Q Imbalance in Low-IF Transmitters

For the low-IF transmitters, the desired signal is located at an intermediate frequency and the image signal created after upconversion appears on the other side of the carrier frequency and causes interference with the other channels signals. For a multichannel scenario, where several signals with different power levels are received as a whole, the image signal for some channels can be 50-100dB stronger than the desired signal and the interference signal may completely mask the desired signal. Thus, the image attenuation of 20-40dB provided by the modern analog electronics is clearly not sufficient for architectures with low-IF topology and some kind of mitigation component is necessary. Figure 3.8 presents the case of two low-IF signals, with their centre frequencies equal to image frequency of each other, transmitted with 2% gain imbalance and 10^{o} phase imbalance. The signal located at positive IF frequency is 16-QAM modulated and the other signal at negative IF frequency is QPSK modulated. The power difference between the two channel signals is 10dB. The weaker channel located at negative IF frequency, after I/Q imbalance, is detected and its constellation is plotted in Figure 3.8-b. As can be observed that there is a large degradation even for a small imbalance values and the signal can no longer be detected correctly.

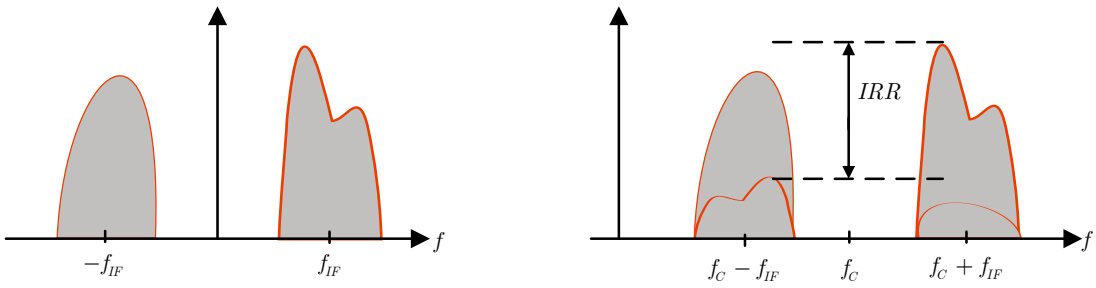

(a) *(b)*

Figure 3.7: *A spectral illustration of the impact of I/Q imbalance in low-IF conversion transmitters with desired signal located at an intermediate frequency* $-f_{IF}$ *and an image signal located at* f_{IF} *(a) IF signal (b) RF signal after upconversion. The cross talk between the desired and image signal is due to I/Q imbalance.*

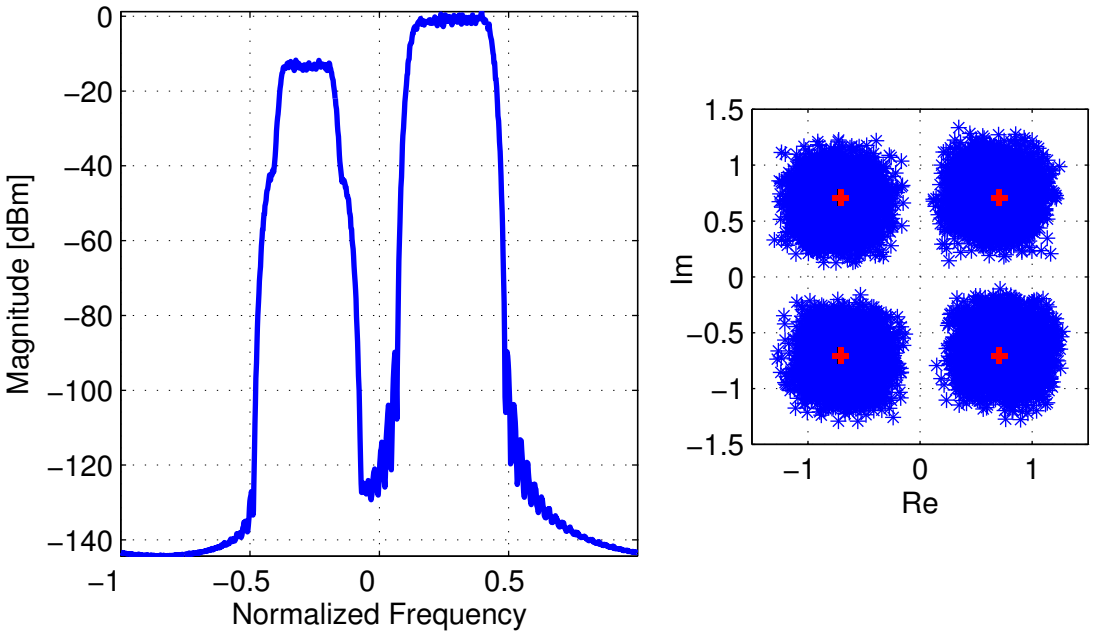

(a) *(b)*

Figure 3.8: *Effect of I/Q imbalance in low-IF transmitters (a) spectrum of imbalanced low-IF signals (b) constellation diagram plotted after detecting the signal located at negative IF frequency.*

3.5 Widely-Linear Pre-distortion Based Approach

The complex imbalanced baseband signal $z(t)$ in (3.9) is not a linear function of $x(t)$ but linearly dependent on both $x(t)$ and $x^*(t)$ and is called widely linear (WL) [23], [25]. Therefore, to predistort $x(t)$, a widely-linear estimator of the following form can be used.

$$x_P(t) = w_1(t) * x(t) + w_2(t) * x^*(t) \tag{3.24}$$

Here $x(t) = x_I(t) + jx_Q(t)$. Since the main source of trouble is the conjugate signal produced due to the I/Q imbalance, it is sufficient to only suppress the conjugate term in (3.9) and the compensator reduces to the form [23]

$$x_P(t) = x(t) + w(t) * x^*(t) \tag{3.25}$$

where $w(t)$ denotes the pre-distorter impulse response. Substituting (3.25) in (3.9)yields the pre-distorted imbalanced signal as

$$z_P(t) = g_{1,T}(t) * x_P(t) + g_{2,T}(t) * x_P^*(t) \tag{3.26}$$

$$z_P(t) = g_{1,T}(t) * \Big(x(t) + w(t) * x^*(t)\Big) + g_{2,T}(t) * \Big(x(t) + w(t) * x^*(t)\Big)^* \tag{3.27}$$

$$\begin{aligned} z_P(t) = {} & x(t) * \Big(g_{1,T}(t) + g_{2,T}(t) * w^*(t)\Big) + \\ & x^*(t) * \Big(g_{1,T}(t) * w(t) + g_{2,T}(t)\Big) \end{aligned} \tag{3.28}$$

The conjugate term can be suppressed by setting $g_{1,T}(t) * w(t) + g_{2,T}(t) = 0$, which can be achieved with a pre-distortion filter, in frequency domain, of the form [23]

$$W_{OPT}(f) = -\frac{G_{2,T}(f)}{G_{1,T}(f)} \tag{3.29}$$

The above optimum compensator is able to completely suppress the mirror frequency interference provided that the imbalance filters $g_{1,T}(t)$ and $g_{2,T}(t)$ are estimated properly. However, imbalance filters are function of gain, phase, and DAC frequency response (equation (3.8)) and in practice it is impossible to determine these parameters accurately. Therefore, there is always a residual image signal present. But it does not harm the performance of a system as long as the achieved image signal attenuation meets the radio specifications.

From (3.28), the IRR after pre-distortion can be described as

$$IRR_{PD}(f)[dB] = 10\log_{10}\left(\frac{\left|G_{1,T}(f) + G_{2,T}(f)W^*(-f)\right|^2}{\left|G_{1,T}(f)W(f) + G_{2,T}(f)\right|^2}\right) \tag{3.30}$$

The general structure of a direct conversion transmitter utilizing the I/Q compensator is delineated in Figure 3.9. The I/Q compensator is based on (3.25) and the coefficients of pre-distortion filter are estimated using WLLS technique, which is discussed later in this section. The feedback loop is employed to estimate the I/Q imbalance caused by the up-converter components such as DAC, LPF, mixers, and modulators.

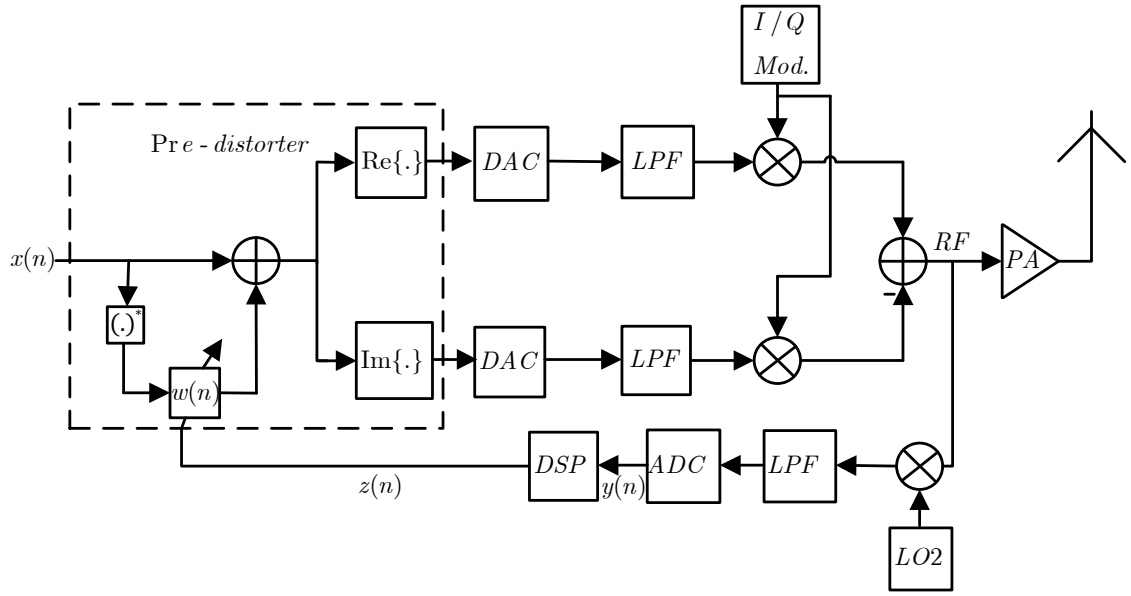

Figure 3.9: *A block diagram of IQ upconversion based transmitter with pre-distorter to compensate for I/Q imbalance. The coefficients of pre-distortion filter* $w(n)$ *are estimated using WLLS technique with the aid of feedback loop.*

At the start-up, the pre-distorter is switched off and the digital I- and Q- data are converted to analog baseband signals by DAC. Baseband signals, after low-pass filtering, are up-converted to RF frequency by I/Q modulator. In the estimation phase [23], imbalanced RF signal is first down-converted to an low-intermediate frequency. The LO used at this stage is real to avoid any additional I/Q imbalance. LPF is then used to preserve the desired and image signals and the signal after filtering is sampled by ADC. The sampled signal is then processed digitally for translation to baseband. Given single mixer feedback loop processing is performed to obtain a perfect estimate of the baseband equivalent of actual I/Q modulator output. The coefficients of pre-distortion filter are then estimated using the original and feedback signal. Finally, in the calibration phase [23], [24], baseband I- and Q- data are pre-distorted and are transmitted. The general structure of a pre-distortion based direct conversion transmitter is shown in Figure 3.9.

One might expect that the translation of a signal from RF to baseband in the feedback can be performed without any error. But, in practice, the feedback signal is exposed to a variety of errors. These errors include non-ideal frequency response of feedback loop, LO signal leakage, and frequency and timing synchronization errors [23]. It will be shown at the end of this section that the effects of non-ideal frequency response of

feedback loop is cancelled while estimating the pre-distortion filter and it is not needed to determine it. Synchronization between transmitted and feedback data is a fundamental requirement for the given pre-distortion based transmitters. Synchronization process has different aspects such as frequency synchronization and timing synchronization [26]. Frequency synchronization errors lead to the time-varying rotation of the signal constellation points and it can be achieved here by connecting the up- and down-conversion LOs to a single reference frequency source. Timing synchronization task is needed to perform prior to the detection of symbols. Symbol timing errors introduce intersymbol interference (ISI) to the signal.

As mentioned in the last chapter, direct-upconversion transmitter based on the I/Q modulation principle is subject to LO signal leakage error. It results due to finite isolation between the LO and RF ports of the modulator and a certain amount of LO signal leaks to the RF port and appears at the centre frequency of the modulator. When the RF signal is down converted, LO leakage causes DC offset which can corrupt the baseband modulated signal and also bias the pre-distortion filter estimates [1], [17]. The DC offset can be mitigated by removing the sample mean of the feedback data.

The observed feedback signal after has the form

$$y(t) = g_{fb} e^{j\theta_{fb}} h_{fb}(t) * \left(g_{1,T}(t) * x_P(t) + g_{2,T}(t) * x_P^*(t) \right) \tag{3.31}$$

$$y(t) = \tilde{g}_{1,T}(t) * x_P(t) + \tilde{g}_{2,T}(t) * x_P^*(t) \tag{3.32}$$

where

$$\begin{aligned} \tilde{g}_{1,T}(t) &= g_{fb} e^{j\theta_{fb}} h_{fb}(t) * g_{1,T}(t) \\ \tilde{g}_{2,T}(t) &= g_{fb} e^{j\theta_{fb}} h_{fb}(t) * g_{2,T}(t) \end{aligned} \tag{3.33}$$

In (3.33), parameters $\{g_{fb}, e^{j\theta_{fb}}, h_{fb}(t)\}$ model the unknown gain, phase, and impulse response of the feedback loop. The optimum pre-distortion filter based on (3.32) then has the form

$$\tilde{W}(f) = -\frac{ge^{j\theta}H_{fb}(f)G_{2,T}(f)}{ge^{j\theta}H_{fb}(f)G_{1,T}(f)} = -\frac{G_{2,T}(f)}{G_{1,T}(f)} = W_{OPT}(f) \tag{3.34}$$

The above equation has similar form as (3.29), hence, there is no need to estimate the actual imbalance filters $g_{1,T}(t)$ and $g_{2,T}(t)$, but to estimate $\tilde{g}_{1,T}(t)$ and $\tilde{g}_{2,T}(t)$, as the effect of feedback loop is cancelled out while computing the coefficients of optimum pre-distortion filter [23].

With proper data conditioning i.e. matching the feedback signal $y(t)$ with original input signal $x(t)$ in time and normalizing the measured signal to have the same power as the original signal, the observed feedback signal is equivalent to the complex envelope of the transmitted RF signal $z(t)$. Thus, from now on, $z(t)$ will be used for the measured signal instead of $y(t)$.

Now, we address the problem of estimating the pre-distortion filter with the aid of a feedback loop. The WLLS approach is based on fitting the measured and original baseband data to determine the imbalance filter coefficients. From now on, the data samples are written in vector form to simplify the derivation.

The original baseband signal vector and the imbalance impulse response vector has the form

$$\mathbf{x}(n) = \begin{bmatrix} x(n) & x(n-1) & \dots & x(n-L+1) \end{bmatrix}^T$$

$$\tilde{\mathbf{g}}_{i,T} = \begin{bmatrix} \tilde{g}_{i,T,1} & \tilde{g}_{i,T,2} & \dots & \tilde{g}_{i,T,N_g} \end{bmatrix}^T$$

where L is the length of measured data, N_g is the length of the imbalance filters $\tilde{g}_{1,T}, \tilde{g}_{2,T}$ and $i = 1,2$. The pre-distortion filter $\mathbf{w}$ is a column vector of length N, initially containing only zeros.

$$\mathbf{w} \overset{\Delta}{=} \begin{bmatrix} w_1 & w_2 & \dots & w_N \end{bmatrix}^T$$

The optimum length N_W of the pre-distortion filter will be determined after simulation and measurement results.

The feedback signal $z(n)$ is of the form

$$\mathbf{z}(n) = \mathbf{X}(n)\tilde{\mathbf{g}}_{1,T} + \mathbf{X}^*(n)\tilde{\mathbf{g}}_{2,T} = \left[\mathbf{X}(n) \mid \mathbf{X}^*(n)\right]\begin{bmatrix}\tilde{\mathbf{g}}_{1,T}\\ \tilde{\mathbf{g}}_{2,T}\end{bmatrix} = \mathbf{X}_b(n)\begin{bmatrix}\tilde{\mathbf{g}}_{1,T}\\ \tilde{\mathbf{g}}_{2,T}\end{bmatrix} \tag{3.35}$$

Here, $\mathbf{X}(n)$ is the convolution matrix formed from $x(n)$ and $\mathbf{z}(n) = [z(n)\ z(n-1)\ \ldots\ z(n-L+1)]^T$, and L is the length of the measured data block. From (3.35) the imbalance filters can be computed using the following equation

$$\begin{bmatrix}\tilde{\mathbf{g}}_{1,T}\\ \tilde{\mathbf{g}}_{2,T}\end{bmatrix} = \mathbf{X}^+(n)\mathbf{z}(n) \tag{3.36}$$

where $\mathbf{X}^+(n)$ is the pseudo-inverse of $\mathbf{X}(n)$ which has following form [26]

$$\mathbf{X}(n) = \begin{bmatrix} x(n-N_W+1) & x(n-N_W+2) & \ldots & x(n) \\ x(n-N_W) & x(n-N_W+1) & \ldots & x(n-1) \\ \vdots & \vdots & \ddots & \vdots \\ x(n-N+1) & x(n-N) & \cdots & x(n-N-N_W) \end{bmatrix} \tag{3.37}$$

If $\mathbf{X^H}(n)\mathbf{X}(n)$ is invertible, the pseudo-inverse takes the familiar form $\mathbf{X}^+(n) = \left(\mathbf{X}^H(n)\mathbf{X}(n)\right)^{-1}\mathbf{X}^H(n)$ as is well-known from the estimation literature [23].

After estimating the imbalance filters, the next task is to determine the pre-distortion filter. The pre-distortion filter can be computed by taking the ratio of the Fourier transforms of imbalance filters $\tilde{g}_{1,T}, \tilde{g}_{2,T}$ as described in equation (3.29). Alternatively, it can be derived in the time-domain form. The weighting factor of the conjugate term in (3.28) has vector form

$$\tilde{\mathbf{g}}^{0}_{2,T} + \tilde{\mathbf{G}}_{1,T}\,\mathbf{w} = 0$$

Solving the above yields the pre-distortion filter as

$$\mathbf{w} = -\left(\tilde{\mathbf{G}}_{1,T}^{H}\,\tilde{\mathbf{G}}_{1,T}\right)^{-1}\tilde{\mathbf{G}}_{1,T}^{H}\,\tilde{\mathbf{g}}_{2,T}^{0} \tag{3.38}$$

where $\tilde{\mathbf{G}}_{1,T}$ is the convolution matrix formed from $\tilde{\mathbf{g}}_{1,T}$ and $\tilde{\mathbf{g}}_{2,T}^{0} = [\tilde{\mathbf{g}}_{2,T}^{T}\ 0\ \ldots\ 0]^{T}$ is a zero-padded version of $\tilde{\mathbf{g}}_{2,T}$, with N-1 zeros attached to its end.

Once the pre-distortion filter is determined, it is used to pre-distort the signal. Narrow spectral support of transmit signal may result in ill-conditioning of $\mathbf{X}_b^H(n)\mathbf{X}_b(n)$, which can be alleviated by adding a low-level white circular noise to $x(n)$ during the estimation. This corresponds to the diagonal loading of $\mathbf{X}_b^H(n)\mathbf{X}_b(n)$, and it will effectively make the matrix better conditioned [23].

3.6 Post-Inverse Estimation Based Approach

The technique developed by Ding et al. [24] is based on finding the inverse of the path in the modulator which causes the I/Q imbalance. With the estimate of imbalance filters, the I/Q compensator can be constructed as a cascade of four real compensation filters and channel filters. The complete model of the pre-distortion based transmitter is depicted in Figure 3.10.

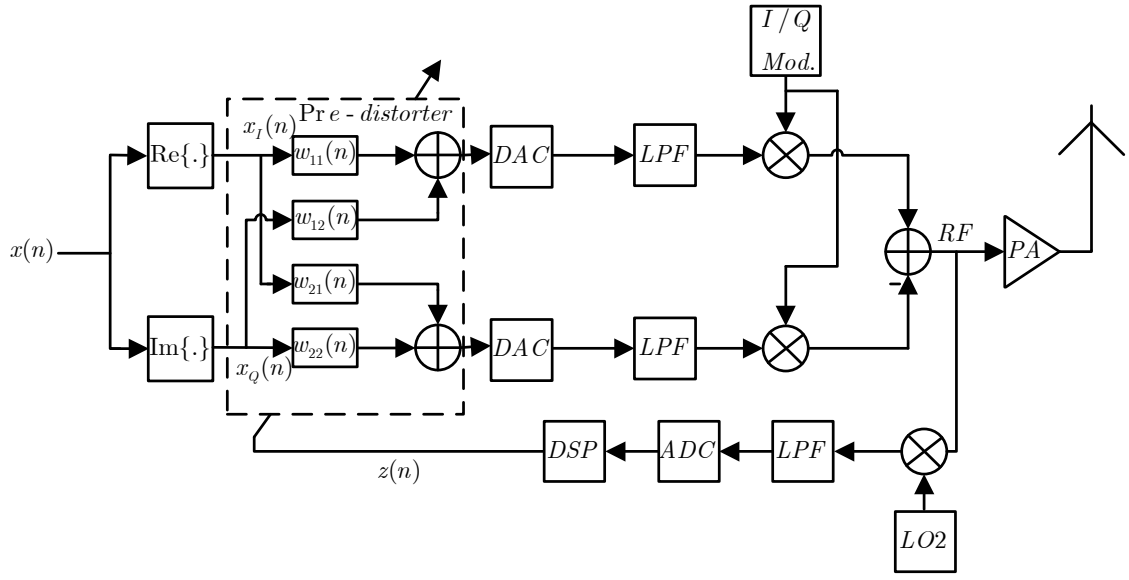

Figure 3.10: *A block diagram of I/Q up-conversion based transmitter with pre-distorter. The coefficients of pre-distortion filters* w *are estimated using post-inverse estimation technique with the aid of feedback loop.*

To derive the IRR expression for post-inverse estimation based technique, consider the baseband signal which after pre-distortion is given by

$$x_P(t) = x_I(t) * \left(w_{11}(t) + jw_{21}(t)\right) + x_Q(t) * \left(w_{12}(t) + jw_{22}(t)\right)$$

$$x_P(t) = x_I(t) * w_I(t) + x_I(t) * w_Q(t) \tag{3.39}$$

where $w_I = w_{11} + jw_{21}; w_Q = w_{12} + jw_{22}$ are the complex pre-distortion filters and $x_I(t); x_Q(t)$ are the in-phase and quadrature component of the input signal. The above equation can also be expressed in terms of input signal $x(t)$ and its complex conjugate $x^*(t)$ as

$$x_P(t) = x(t) * \left(\frac{w_I(t) - jw_Q(t)}{2}\right) + x^*(t) * \left(\frac{w_I(t) + jw_Q(t)}{2}\right) \tag{3.40}$$

The baseband equivalent of pre-distorted RF signal is

$$z_P(t) = x_P(t) * g_D(t) + x_P^*(t) * g_M(t) \tag{3.41}$$

$$\begin{aligned} z_P(t) = &\left(x(t) * \left(\frac{w_I(t) - jw_Q(t)}{2}\right) + x^*(t) * \left(\frac{w_I(t) + jw_Q(t)}{2}\right)\right) * g_D(t) + \\ &\left(x(t) * \left(\frac{w_I(t) - jw_Q(t)}{2}\right) + x^*(t) * \left(\frac{w_I(t) + jw_Q(t)}{2}\right)\right)^* * g_M(t) \end{aligned} \tag{3.42}$$

After some mathematical derivations, the above equation simplifies to

$$\begin{aligned} z_P(t) = x(t) * &\left(w_D(t) * g_D(t) + w_M^*(t) * g_M(t)\right) + \\ &x^*(t) * \left(w_M(t) * g_D(t) + w_D^*(t) * g_M(t)\right) \end{aligned} \tag{3.43}$$

Where $w_D(t)$ and $w_M(t)$ are, respectively, the direct and image transfer functions of the pre-distortion filters and are given by

$$\begin{aligned} w_D(t) &= \frac{w_I(t) - jw_Q(t)}{2} \\ w_M(t) &= \frac{w_I(t) + jw_Q(t)}{2} \end{aligned} \tag{3.44}$$

The IRR after pre-distortion is thus

$$IRR_{PD}(f)[dB] = 10\log_{10}\left(\frac{\left|W_D(f)G_D(f) + W_M^*(-f)G_M(f)\right|^2}{\left|W_M(f)G_D(f) + W_D^*(-f)G_M(f)\right|^2}\right) \tag{3.45}$$

Now, in order to derive an expression for the pre-distortion filters, assume that all four imbalance filters have same length K. The discrete form of the baseband equivalent RF signal of (3.15) is then

$$z(n) = \sum_{K=0}^{K-1}\left(x_I(n-K)g_I(k) + x_Q(n-K)g_Q(k)\right) \tag{3.46}$$

For a block of $x(n)$ and $z(n)$ data samples, (3.46) can be written in vector form as

$$\mathbf{z} = \mathbf{X_I}\mathbf{g_I} + \mathbf{X_Q}\mathbf{g_Q} \tag{3.47}$$

Where $\mathbf{z} = [z(k - L - 1)\ldots z(N - L - 1)]^T$ with L a selectable delay, $\mathbf{X}_I = \mathrm{Re}(\mathbf{X})$ and $\mathbf{X}_Q = \mathrm{Im}(\mathbf{X})$ with

$$\mathbf{X} = \begin{bmatrix} x(K-1) & x(K-2) & \ldots & x(0) \\ x(K) & x(K-1) & \ldots & x(1) \\ \vdots & \vdots & \ddots & \vdots \\ x(N-1) & x(N-2) & \cdots & x(N-K) \end{bmatrix} \tag{3.48}$$

and

$$\mathbf{g_I} = [g_I(0)\ \cdots\ g_I(K-1)]^T$$
$$\mathbf{g_Q} = [g_Q(0)\ \cdots\ g_Q(K-1)]^T$$

The cost function to find the imbalance filter coefficients is [24]

$$J(\mathbf{g_I}, \mathbf{g_Q}) = \left\|\mathbf{z} - \mathbf{X_I}\mathbf{g_I} - \mathbf{X_Q}\mathbf{g_Q}\right\|^2 \tag{3.49}$$

Where $\|.\|^2$ denotes the l_2 norm of a vector. The optimal channel coefficients that minimize the cost function can be found by setting the partial derivatives of J with respect to $\mathbf{g}_\mathbf{I}^* \mathbf{g}_\mathbf{Q}^*$ to zero, i.e., [24]

$$\frac{\partial J}{\partial \mathbf{g}_\mathbf{I}^*} = \mathbf{X}_\mathbf{I}^\mathbf{H}\left(\mathbf{z} - \mathbf{X}_\mathbf{I}\mathbf{g}_\mathbf{I} - \mathbf{X}_\mathbf{Q}\mathbf{g}_\mathbf{Q}\right) = \mathbf{0} \tag{3.50}$$

$$\frac{\partial J}{\partial \mathbf{h}_\mathbf{Q}^*} = \mathbf{X}_\mathbf{Q}^\mathbf{H}\left(\mathbf{z} - \mathbf{X}_\mathbf{I}\mathbf{g}_\mathbf{I} - \mathbf{X}_\mathbf{Q}\mathbf{g}_\mathbf{Q}\right) = \mathbf{0} \tag{3.51}$$

Since $\mathbf{X}_\mathbf{I}^\mathbf{H}, \mathbf{X}_\mathbf{I}^\mathbf{H}$ are real matrices, thus the Hermitian transpose can be replaced by a simple transpose and above two equations simplifies to [24]

$$\begin{bmatrix} \mathbf{X}_\mathbf{I}^\mathbf{T}\mathbf{X}_\mathbf{I} & \mathbf{X}_\mathbf{I}^\mathbf{T}\mathbf{X}_\mathbf{Q} \\ \mathbf{X}_\mathbf{Q}^\mathbf{T}\mathbf{X}_\mathbf{I} & \mathbf{X}_\mathbf{Q}^\mathbf{T}\mathbf{X}_\mathbf{Q} \end{bmatrix} \begin{bmatrix} \mathbf{g}_\mathbf{I} \\ \mathbf{g}_\mathbf{Q} \end{bmatrix} = \begin{bmatrix} \mathbf{X}_\mathbf{I}^\mathbf{T}\mathbf{z} \\ \mathbf{X}_\mathbf{Q}^\mathbf{T}\mathbf{z} \end{bmatrix} \tag{3.52}$$

Therefore, the Least Squares (LS) estimate of the $\mathbf{g}_\mathbf{I}, \mathbf{g}_\mathbf{Q}$ are [24]

$$\begin{bmatrix} \hat{\mathbf{g}}_\mathbf{I} \\ \hat{\mathbf{g}}_\mathbf{Q} \end{bmatrix} = \begin{bmatrix} \mathbf{X}_\mathbf{I}^\mathbf{T}\mathbf{X}_\mathbf{I} & \mathbf{X}_\mathbf{I}^\mathbf{T}\mathbf{X}_\mathbf{Q} \\ \mathbf{X}_\mathbf{Q}^\mathbf{T}\mathbf{X}_\mathbf{I} & \mathbf{X}_\mathbf{Q}^\mathbf{T}\mathbf{X}_\mathbf{Q} \end{bmatrix}^{-1} \begin{bmatrix} \mathbf{X}_\mathbf{I}^\mathbf{T}\mathbf{z} \\ \mathbf{X}_\mathbf{Q}^\mathbf{T}\mathbf{z} \end{bmatrix} \tag{3.53}$$

As described at the end of section 3.5, the estimation can be made more accurate by adding a low level noise to both $x(n)$ and $z(n)$. Thus, after using a low level white noise with zero mean and variance σ^2, (3.53) becomes [24]

$$\begin{bmatrix} \hat{\mathbf{g}}_\mathbf{I} \\ \hat{\mathbf{g}}_\mathbf{Q} \end{bmatrix} = \begin{bmatrix} \mathbf{X}_\mathbf{I}^\mathbf{T}\mathbf{X}_\mathbf{I} + \mathbf{z}^2\mathbf{I} & \mathbf{X}_\mathbf{I}^\mathbf{T}\mathbf{X}_\mathbf{Q} \\ \mathbf{X}_\mathbf{Q}^\mathbf{T}\mathbf{X}_\mathbf{I} & \mathbf{X}_\mathbf{Q}^\mathbf{T}\mathbf{X}_\mathbf{Q} + \mathbf{z}^2\mathbf{I} \end{bmatrix}^{-1} \begin{bmatrix} \mathbf{X}_\mathbf{I}^\mathbf{T}\mathbf{z} + \mathbf{z}^2\mathbf{e} \\ \mathbf{X}_\mathbf{Q}^\mathbf{T}\mathbf{z} + \mathbf{z}^2\mathbf{e} \end{bmatrix} \tag{3.54}$$

Where $\mathbf{I}$ is the $K \times K$ identity matrix, and $\boldsymbol{e} = [\mathbf{0}_L^T \ 1 \ \mathbf{0}_M^T]^T$ where $\mathbf{0}_L^T$ and $\mathbf{0}_M^T$ are, respectively, length L and $M = K - L - 1$ column vector filled with all zeros.

The compensator is the pre-inverse of the path from reconstruction filter to the modulator output. However, assuming this path to be a linear system, the pre-inverse is

same as the post-inverse. Therefore, the I/Q compensator can be obtained using (3.53) by treating $z(n)$ as the input and $x(n)$ as the desired output, i.e. [24]

$$\begin{bmatrix} \mathbf{w}_I \\ \mathbf{w}_Q \end{bmatrix} = \begin{bmatrix} \mathbf{Z}_I^T\mathbf{Z}_I + s^2\mathbf{I} & \mathbf{Z}_I^T\mathbf{Z}_Q \\ \mathbf{Z}_Q^T\mathbf{Z}_I & \mathbf{Z}_Q^T\mathbf{Z}_Q + s^2\mathbf{I} \end{bmatrix}^{-1} \begin{bmatrix} \mathbf{Z}_I^T\mathbf{z} + z^2\mathbf{e} \\ \mathbf{Z}_Q^T\mathbf{z} + z^2\mathbf{e} \end{bmatrix} \tag{3.55}$$

Once the pre-distortion filters are branches, they can be used in (3.39) to pre-distort the baseband signal.

3.7 Discussion

I/Q impairments are unavoidable in the current analog modules and compromise the infinite attenuation of mirror frequencies. This leads to a large degradation of communication waveforms. Luckily, digital signal processing techniques provide an efficient and cheap solution to this problem. In this chapter, the idea of pre-distorting a signal, in such a way that it compensates the mirror frequency interference, prior to transmission is presented. The parameters of the pre-distorter are computed with a feedback signal. Two techniques to estimate the parameters of the pre-distorter are considered. The solution proposed in [23] is based on widely-linear least-square fitting of the output and input data, while, the solution of [24] models the problem of I/Q imbalance with cross coupled real filters and finds their post-inverse. The main advantage of the latter approach is the generation of compensation filters directly from the system's output, whereas, WLLS based approach first estimates the imbalance filters and then computes the pre-distortion filter. The performance of these approaches will be assessed in the next two chapters with simulations and laboratory measurements.

Chapter 4

Simulation Setup and Results

In this chapter, the performance of pre-distortion based compensation schemes presented in Chapter 3 is evaluated with computer simulations. Simulations are performed with MATLAB software. For the WLLS based compensation technique [23], simulation results are illustrated by plotting the IRR curves, which is estimated by finding the imbalanced filters $g_{1,T}(t)$ and $g_{2,T}(t)$ before the I/Q compensation using (3.11) and after I/Q compensation using (3.30) . The results of post-inverse estimation approach [24] are described using IRR expression of (3.45)by signal spectrum.

The chapter is organized into three sections. The first section defines simulation model and parameters of the I/Q imbalance for a real life front-end. The second section presents simulation results. Finally, section 4.3 offers the discussion on the achieved results.

4.1 Simulation Model and Parameters

Simulations are carried out for both single mobile and base-station transmitter cases. The front-end of the transmitter is assumed to be frequency-selective with 3% gain imbalance and 3^{o} phase imbalance, which corresponds to roughly 25-35dB front-end image attenuation within signal bandwidth (Figure 3.1). With the given imbalance parameters, the imbalanced filters $g_{1,T}(t)$ and $g_{2,T}(t)$ are first estimated using (3.8). At beginning, I/Q imbalance is introduced to the original signal with the above estimated imbalance filters using (3.9). The length of imbalance filters is fixed to 3-taps. Algorithms use a block of 25,000 samples of the original and imbalance signal and the pre-distortion filter is estimated by comparing them with each other. The calibration performance of the algorithms is illustrated for pre-distortion filter lengths of 1, 2, and 3- taps. Once the calibration filter is estimated, a new signal waveform is generated and

is pre-distorted. The pre-distorted signal has a form of (3.25) for widely-linear least-square scheme and (3.39) for the post-inverse estimation approach. The IRR is estimated again after I/Q imbalance compensation and the results of 100 independent realizations are averaged and plotted.

4.2 Simulation Results

Simulation results about the transmitter I/Q imbalance calibration are discussed in this section. The first simulation example is based on frequency selective I/Q imabalance model shown in Figure 3.2. In the model, the values of gain and phase imbalance are 3% and 3^{o}, respectively. The plot of IRR without I/Q compensation is presented in Figure 4.1, which shows the frequency selective behavior of image attenuation. For a signal with 15 MHz two-sided bandwidth, the IRR is varying between 25-35dB.

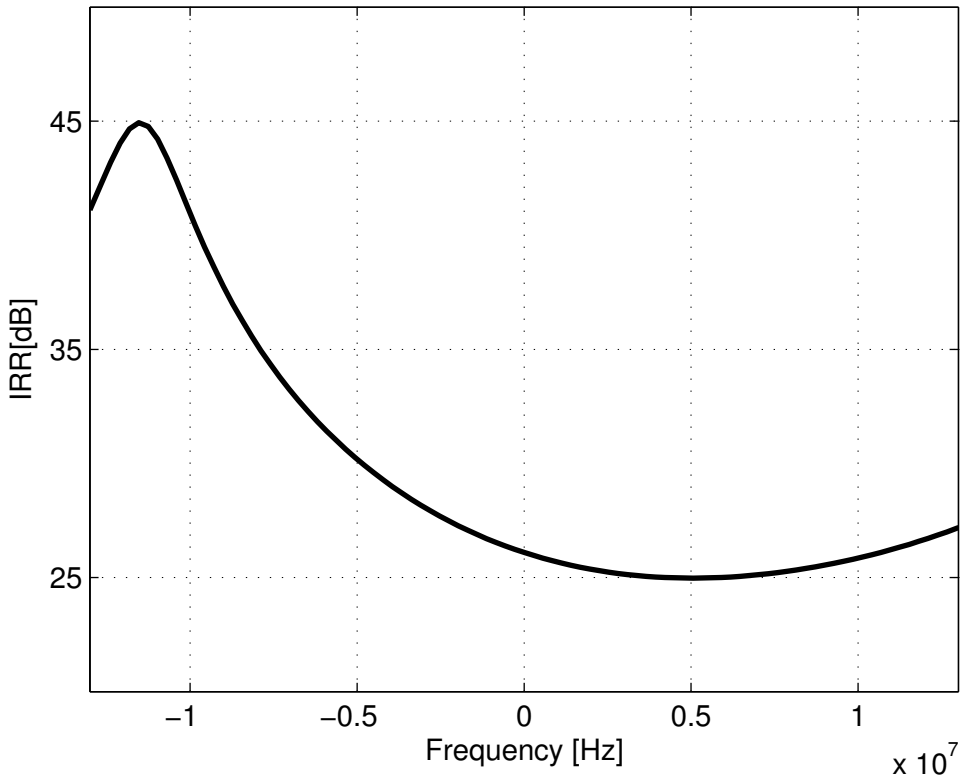

Figure 4.1: *IRR vs. frequency plot of the front-end without calibration.*

The next simulation scenario corresponds to a low-IF signal with 7.5 MHz bandwidth and 4.5 MHz IF frequency. 16-QAM linear modulation scheme is assumed with 6MHz symbol rate and raised-cosine pulse-shaping with 0.25 roll-off factor. I/Q imbalance is

introduced to this signal using (3.9) which reduces the dynamic range to about 25 dB as shown in Figure 4.2.

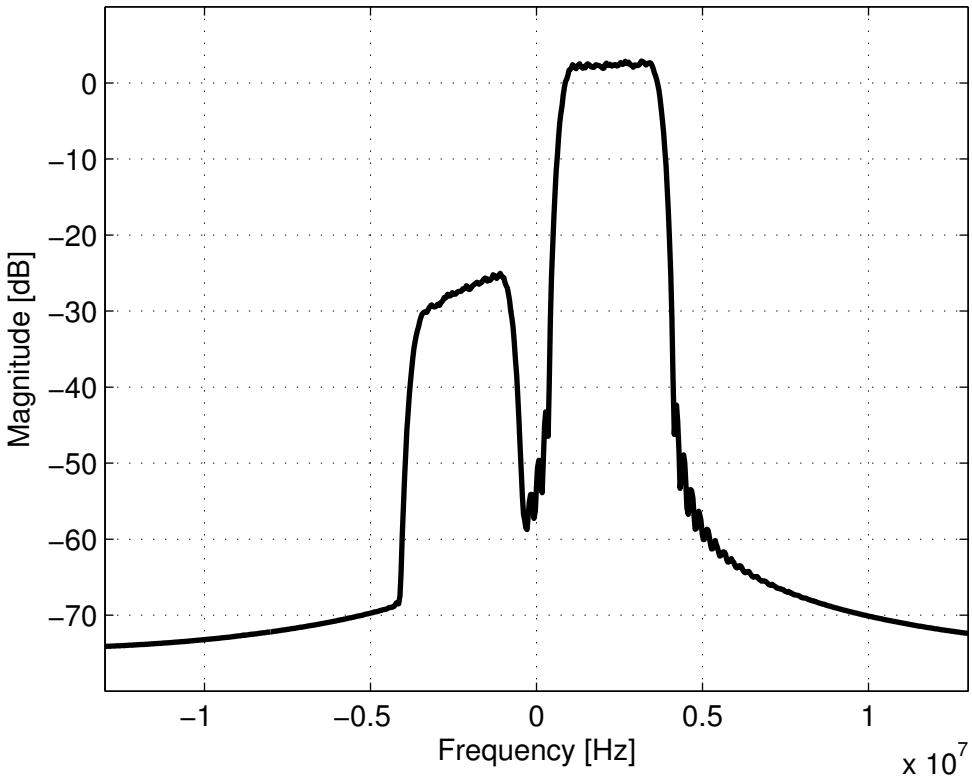

Figure 4.2: *Signal spectrum of a baseband low-IF signal with I/Q imbalance.*

WLLS based calibration method [23] is then applied to correct the I/Q error. A block of 25, 000 samples is used for the estimation of pre-distortion filter. The pre-distorted signal spectrum corresponding to different pre-distortion filter lengths are plotted in Figure 4.3. For the comparison purpose, original signal spectrum is also plotted in the same figure. IRR averaged over 100 independent simulation runs is shown in Figure 4.4. The calibration results for post-inverse estimation technique [24] are shown in Figure 4.5 and Figure 4.6. The results of simulations indicate that image signal power decreases by 25-35 dB as the pre-distortion filter length increases to 3-taps. Hence, it can be said that both techniques can effectively handle the frequency-selective I/Q imbalance and can compensate for I/Q imbalance.

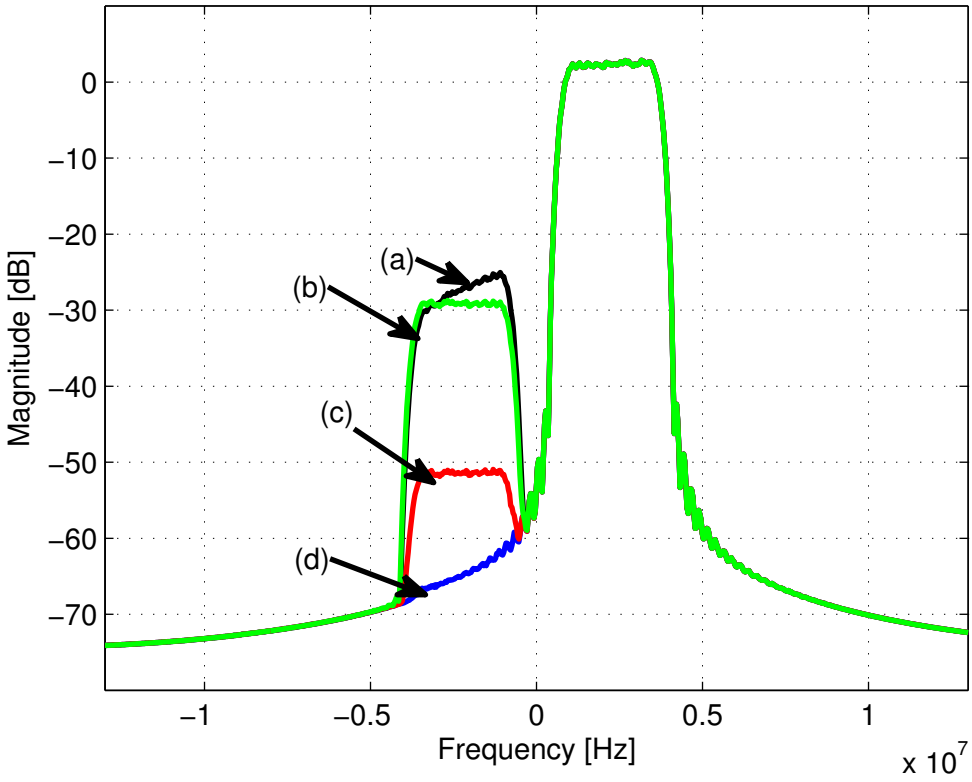

Figure 4.3: *Comparison of signal spectrums before and after I/Q imbalance compensation with different pre-distortion filter lengths. WLLS based compensation technique is used. (a) Uncompensated signal. (b) With a 1-tap pre-distortion filter. (c) With a 2-taps pre-distortion filter. (d) With a 3-taps pre-distortion filter.*

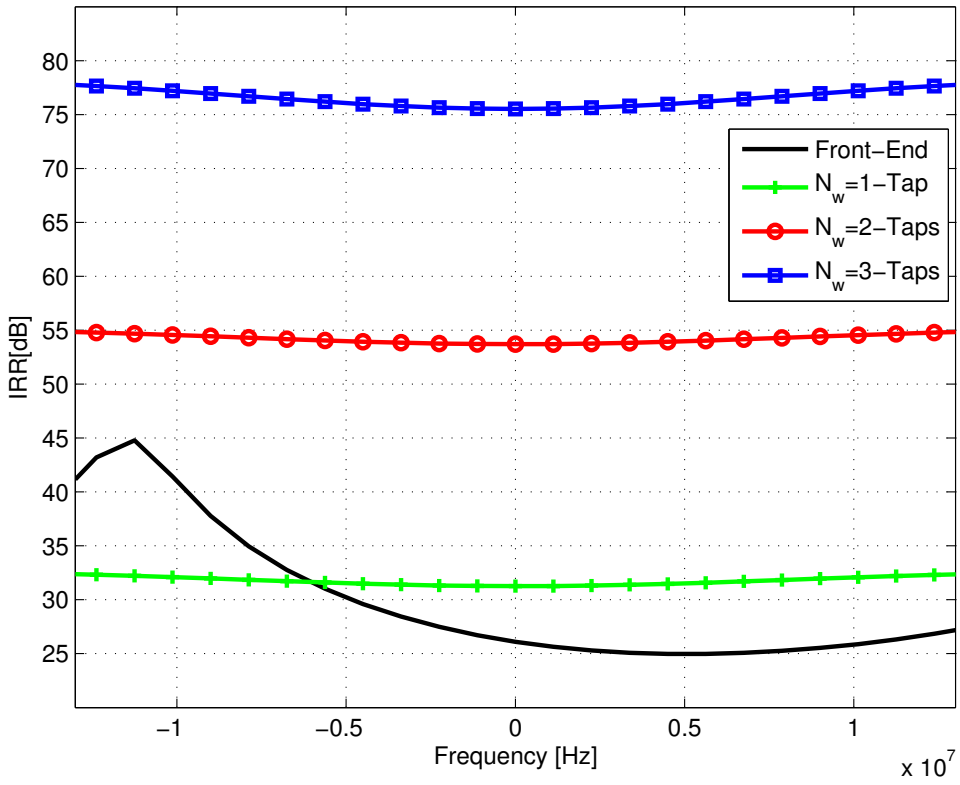

Figure 4.4: *Comparison of IRR curves for low-IF transmitter case without and with I/Q compensation. WLLS based I/Q compensator with different pre-distortion filter length is assumed The signal has 15MHz bandwidth.*

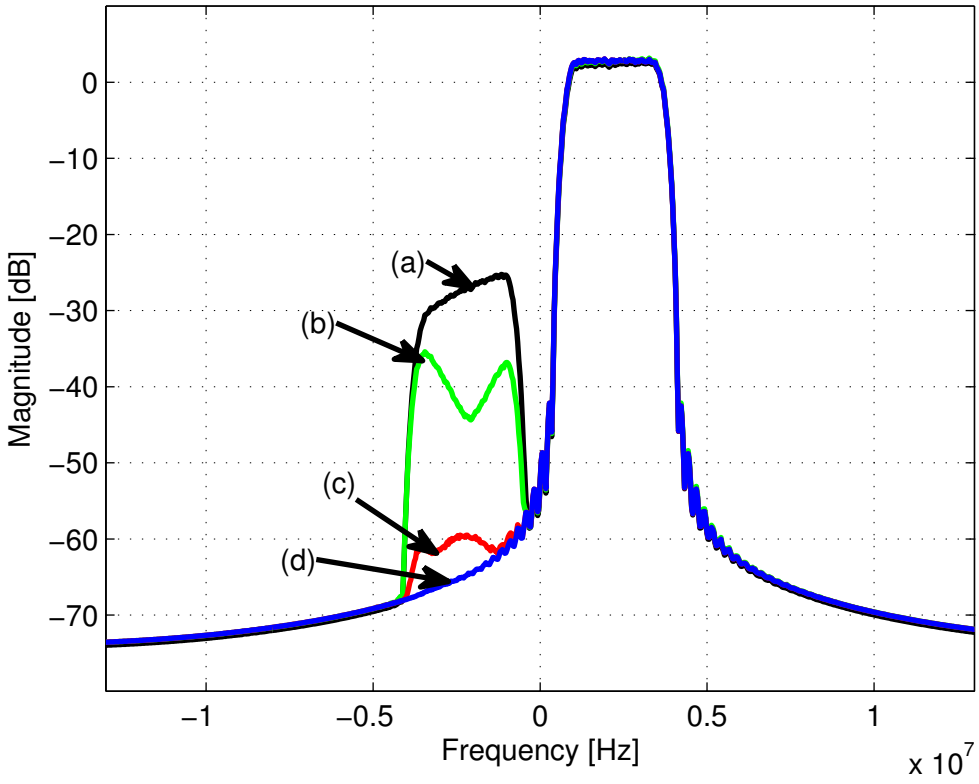

Figure 4.5: *Comparison of signal spectrums before and after I/Q imbalance compensation with different pre-distortion filter lengths. Post-inverse estimation technique is used. (a) Uncompensated signal. (b) With a 1-tap pre-distortion filter. (c) With a 2-taps pre-distortion filter. (d) With a 3-taps pre-distortion filter.*

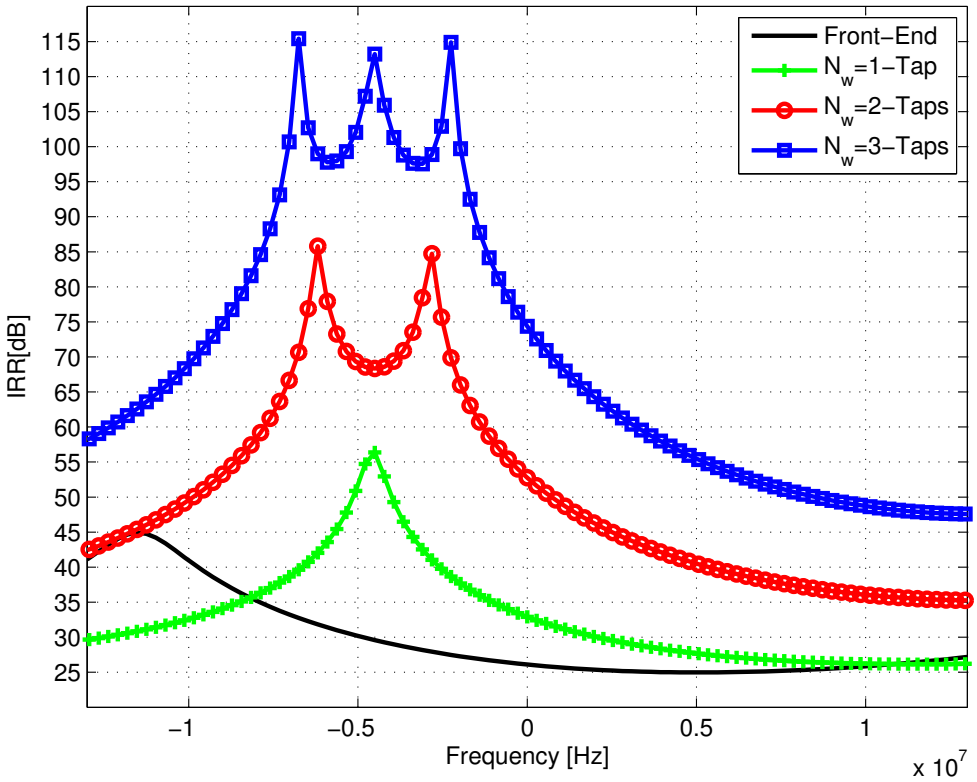

Figure 4.6: *Comparison of IRR curves for low-IF transmitter case without and with I/Q compensation. Post-inverse estimation based I/Q compensator with different pre-distortion filter length is assumed*

The next simulation example considers a wideband signal with 15 MHz two-sided bandwidth and 64-QAM linear modulation type. The symbol rate is 12MHz and the roll-off factor for pulse shaping is 0.25. With the transmitter front-end of Figure 4.1, the obtained results with two I/Q compensation approaches are shown in Figure 4.7 and Figure 4.8.

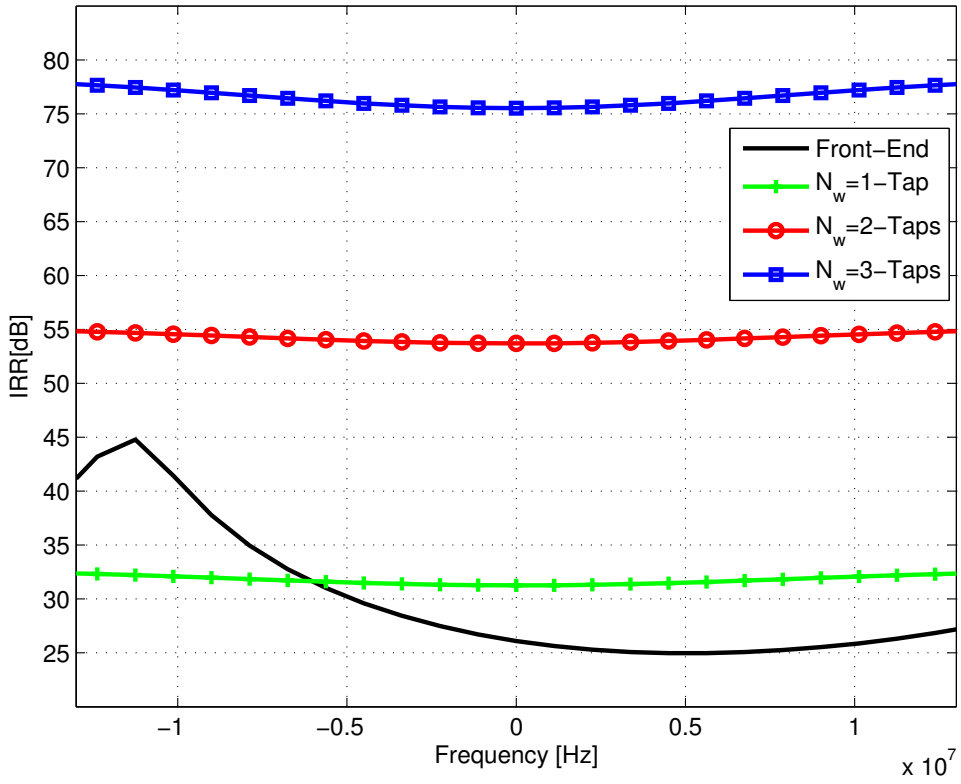

Figure 4.7: *Comparison of IRR vs. frequency curves for direct conversion transmitter case with and without I/Q compensation. WLLS based I/Q compensator with different pre-distortion filter lengths is assumed. The signal has 15MHz bandwidth.*

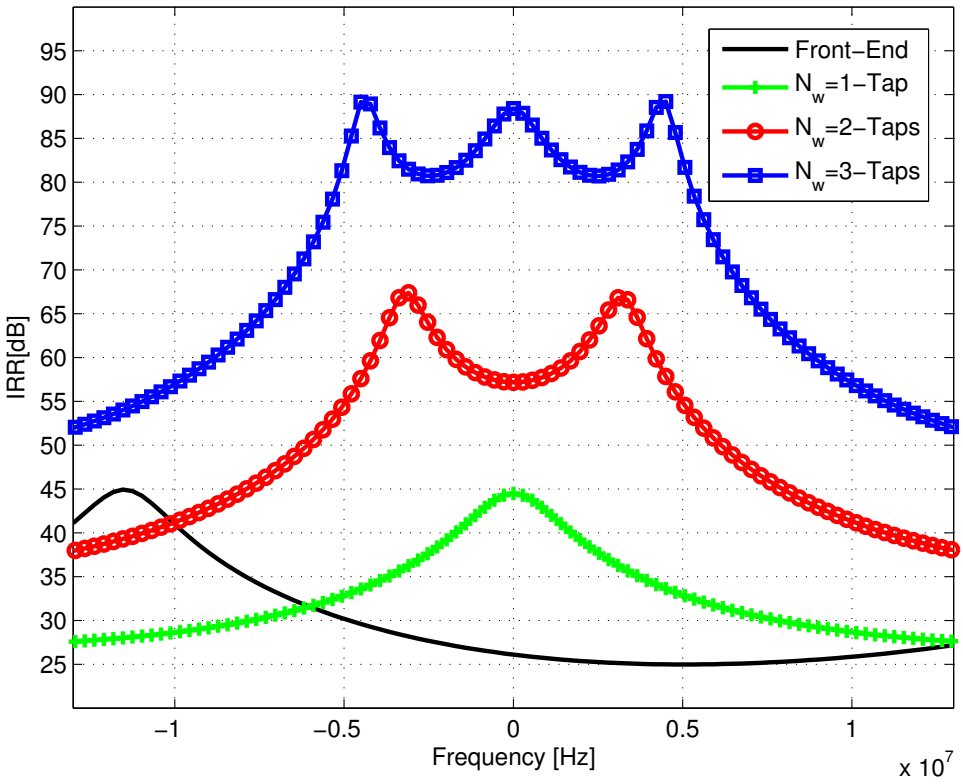

Figure 4.8: *Comparison of IRR vs. frequency curves for direct conversion transmitter case with and without I/Q compensation. Post-inverse estimation based I/Q compensator with different pre-distortion filter lengths is assumed. The signal has 15MHz bandwidth.*

The last example simulates IRR for an OFDM-based transmitter with 64-QAM modulation. Subcarrier spacing is 19.5 KHz and out of total 1024 subcarriers, 768 are active. The front-end IRR is varying between 25-35 dB before compensation and the simulation results (Figure 4.9 and Figure 4.10) evidence that the IRR is clearly improved by using the widely-linear least-square method.

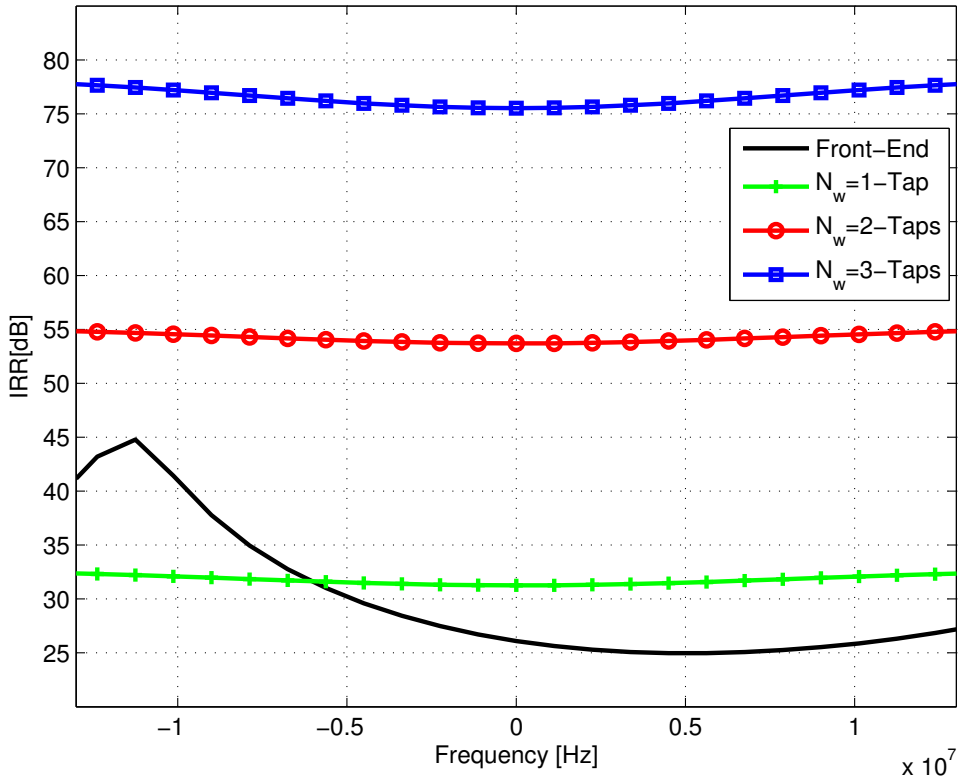

Figure 4.9: *Comparison of IRR vs. frequency curves for the OFDM transmitter case with and without I/Q compensation. WLLS based I/Q compensator with different pre-distortion filter lengths is assumed. The signal has 15 MHz bandwidth.*

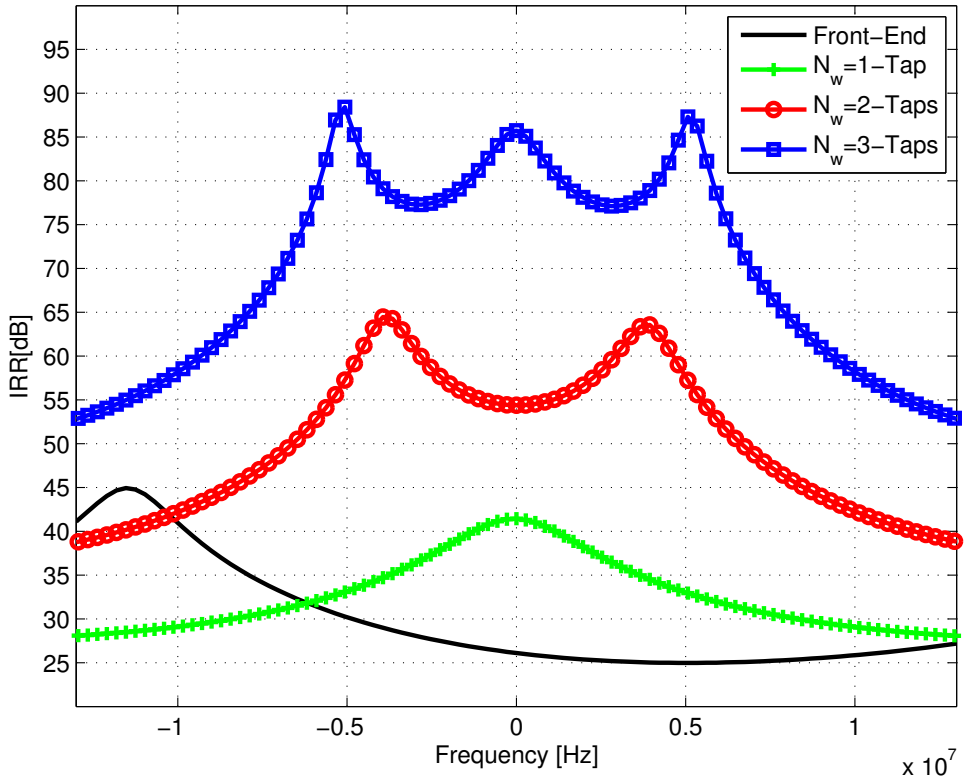

Figure 4.10: *Comparison of IRR vs. frequency curves for the OFDM transmitter case with and without I/Q compensation. Post-inverse estimation based I/Q compensator with different pre-distortion filter lengths is assumed. The signal has 15 MHz bandwidth.*

4.3 Discussion on Results

The performance of two I/Q imbalance compensation algorithms utilizing the so-called widely-linear least-squares model method [23] and post-inverse estimation [24] of the I/Q channel is analyzed with simulations in this chapter. The simulations were carried out with different signal models and the results show that both algorithms are capable of correcting the effects of frequency-selective I/Q imbalance. Comparing the IRR curves of both techniques suggests that WLLS technique performs better than post-inverse estimation techniques by providing flat response over the whole frequency range. The post-inverse estimation based technique gives biased results. The obtained IRR values are more than 60dB with optimum length of pre-distortion filter, which sufficiently fills the RF front-end requirements of most radio transmitters. Simulation results also reveal that the compensation algorithms can also work efficiently with large signal constellation.

Chapter 5

Measurement Setup and Results

This chapter presents a laboratory measurement setup that has been developed to study the impacts of I/Q imbalance in transmitters. The performance of the calibration algorithms discussed in Chapter 3 is also evaluated using this arrangement with various signal types. Although it has been verified with simulations that the pre-distortion algorithms are capable of suppressing the image signals originating due to I/Q imbalance, a practical implementation is necessary to prove that the algorithms can also be used in the real world radio transmitters.

In the first section, an overview of the measurement setup is presented. The next section gives a detailed explanation of the components of measurement setup. The measurement results are illustrated in section 5.3 and a comparison between the simulation and measurement results is made in section 5.4. The chapter ends with the discussion on the achieved results.

5.1 System Development Approach

The generic structure of the whole measurement system is similar to the one shown in Figure 3.9 and Figure 3.10. The hardware is composed of state-of-the-art signal generators, spectrum/signal analyzer and I/Q modulator chip. A block diagram of the setup is illustrated in Figure 5.1.

As shown in the figure, the measurement setup integrates Rohde & Schwarz (R&S) AFQ100A [30] baseband signal generator, HP E4422B [41] RF signal generator, R&S FSG [30] signal and spectrum analyzer, and MAXIM-2023 [31] I/Q up-

downconversion evaluation board. All the instruments are connected to a computer via General Purpose Interface Bus (GPIB) for remote control operation.

Arbitrary waveforms are generated in the computer using Matlab and are loaded to the memory of R&S AFQ 100A baseband signal generator, which outputs the analog I- and Q- signals at its differential ports. The I- and Q- signals are then fed to MAX-2023 I/Q modulator which up-converts the signal to RF frequency. Here, RF frequency source is HP E4422B signal generator. The RF signal is detected by the R&S FSG spectrum analyzer, and down-conversion from RF to baseband is realized by the I/Q subsystem of R&S FSG. A block of sampled data is retrieved from R&S FSG and further processed in the computer for delay estimation and timing error corrections. In the setup, frequency synchronization is achieved by using the reference signal of FSG as a reference oscillator for AFQ and HP signal generators. The calibration filter coefficients are estimated in Matlab using the compensation approaches discussed in Chapter 3, and is used to pre-distort the signal. The pre-distorted signal is again generated by the baseband signal generator and up-converted to the RF frequency. The final results are illustrated with obtained IRR plots, constellation plots, and spectrum of the pre-distorted signal.

5.2 Hardware Description

The aim of this section is to describe the functionalities of the fundamental hardware blocks in the measurement setup. These include R&S AFQ100A baseband signal generator, R&S FSG spectrum/signal analyzer, and MAXIM-2023 I/Q modulator/demodulator.

5.2.1. R&S AFQ 100A I/Q Modulation Generator

R&S AFQ100A [30] is an I/Q modulation baseband signal source, used to generate the test signals during the measurements. The digital baseband waveform data is loaded into the sample memory of the instrument by simulation software such as Matlab. The sample memory size of AFQ 100A is 256M samples. The data is then resampled at the instrument's system rate f_{system}, which can be between 1 KHz to 300 MHz. Resampling the data at the desired symbol rate saves the memory space of the instrument. The dual DACs create the analog signals from the resampled data. This is followed by lowpass

filters which eliminate Nyquist images and noise. AFQ outputs the I/Q signals at the I- and Q- connectors. The maximum I/Q bandwidth offered by R&S AFQ is 100MHz which corresponds to 200MHz RF bandwidth. In addition to the signal generation, AFQ can also introduce impairments to the signal. These impairments include gain, delay, voltage offset, and phase offset. However, this function of R&S AFQ is not used in actual measurements. Figure 5.2 shows block diagram of R&S AFQ with its principle parts.

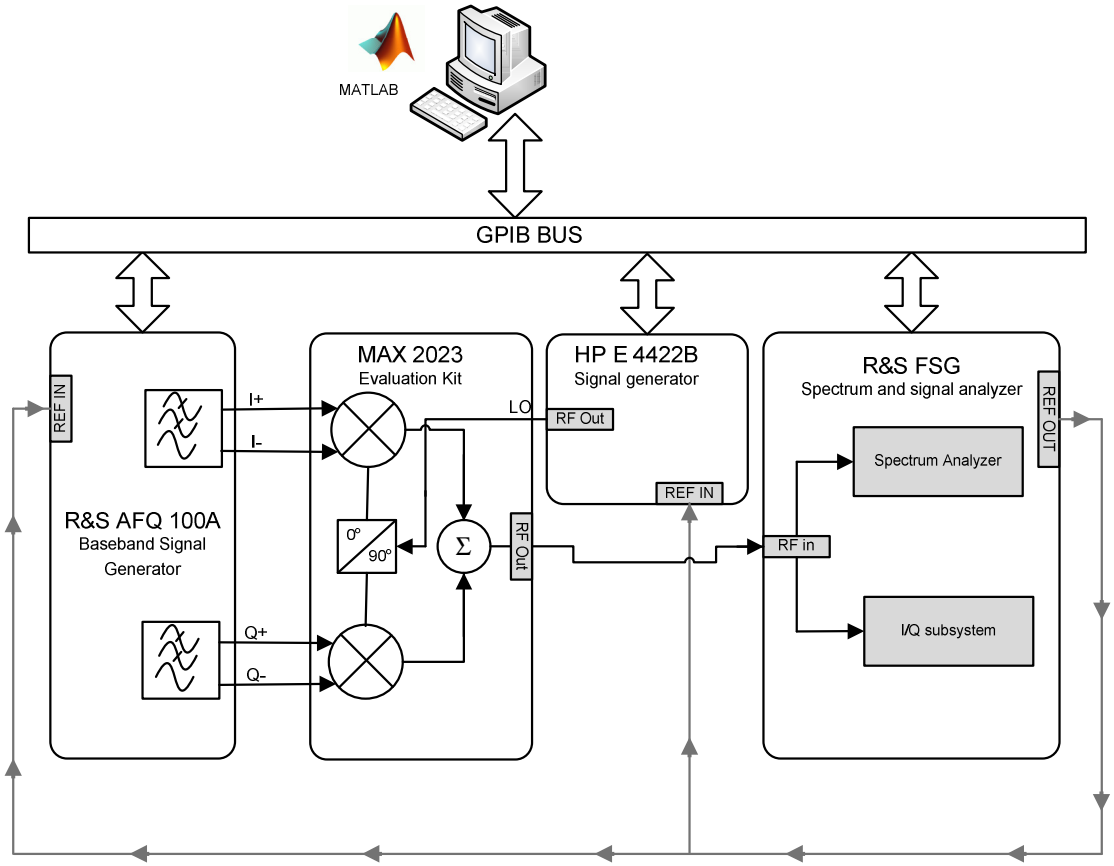

Figure 5.1: *Block diagram of experimental measurement setup consisting of laboratory measurement instruments and MAX2023 I/Q modulator. The instruments are controlled through MATLAB.*

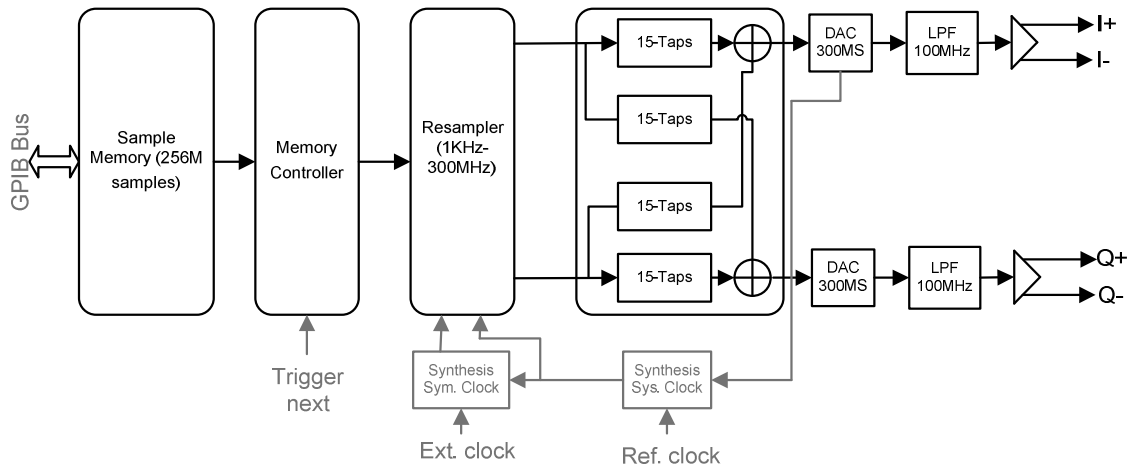

Figure 5.2: *R&S AFQ100A I/Q modulation generator block diagram [30].*

5.2.2. MAX2023 I/Q Modulator/Demodulator Chip

I/Q signals generated by the AFQ are modulated onto RF carrier frequency by MAX2023 [31] direct up- /downconversion modulator/demodulator. The operating frequency range of the chip is between 1500-2300MHz. The filtered baseband signals drive the differential I- and Q- ports of the modulator and the LO port is driven by the HP E4422B signal generator, which provides the desired centre frequency. MAX2023 accepts baseband signals from DC-450MHz with differential amplitudes up to $4V_{peak\text{-}peak}$ and LO between -3dBm to +3dBm. The modulator splits the LO signals into quadrature components. These quadrature components of LO signal are multiplied with the I- and Q- parts of baseband signal and summing them together creates a modulated signal. Non-ideal quadrature splitting of the LO signal and/or gain mismatch between the I- and Q- channels leads to the I/Q imbalance. The typical values of gain and phase mismatch for MAX-2023 chip are 0.025dB and 0.56^{o}, respectively. Also, finite isolation between the LO and RF ports of the chip generates LO leakage signal which appears in the centre of the modulated signal spectrum. The LO leakage of the chip can be determined by terminating the quadrature ports with 50Ω impedance and feeding LO signal at LO port. The output is measured at the RF port.

Measured LO leakage with 0dBm input power level at 1500MHz, 1800MHz, 2000MHz, and 2100MHz is -42dBm, -57dBm, -50dBm, and -50dBm, respectively as delineated in Figure 5.3.

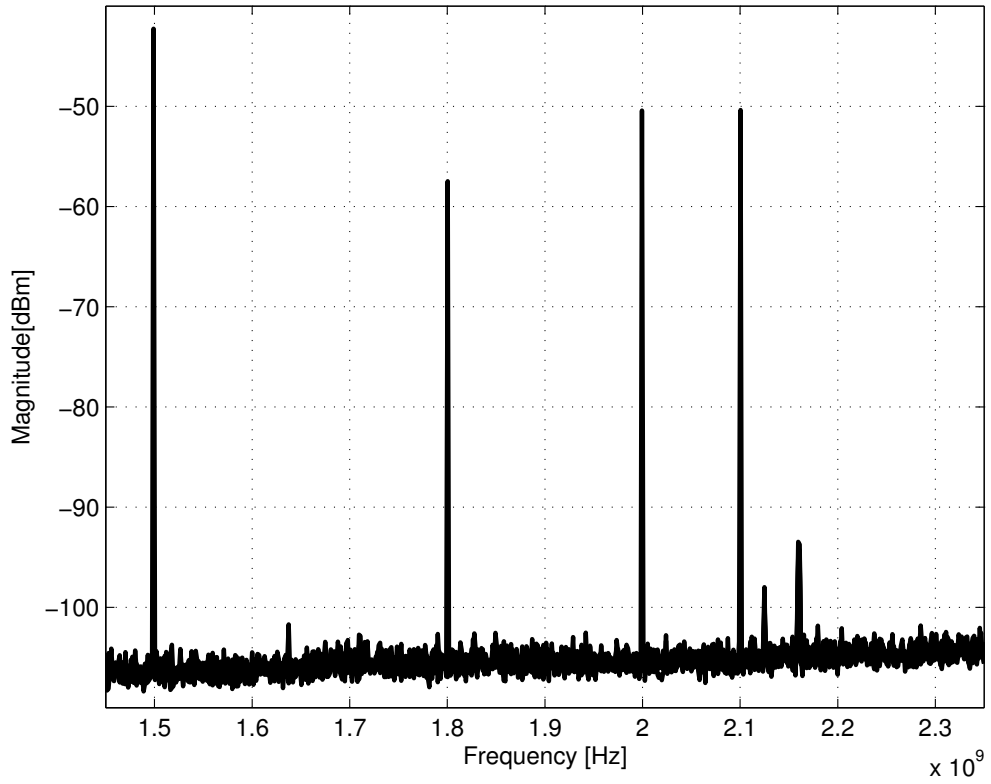

Figure 5.3: *Measurement of LO leakage of MAX2023 chip at various operating frequencies.*

5.2.3. R&S FSG Spectrum and Signal Analyzer

R&S FSG [30] is a spectrum and signal analyzer that is used for spectrum and signal analysis and also for down-converting the signal from RF to baseband. The RF signal from MAX2023 is fed into the RF input port of FSG and it plots the power corresponding to each harmonic component of the signal.

R&S FSG has a built-in I/Q subsystem, shown in Figure 5.4. It is used for collection and output of I/Q measured data. The I/Q subsystem first shifts the RF signal to an intermediate frequency of 20.4MHz and filters it with an IF filter. The bandwidth of the IF filter is selectable from 300KHz to 50MHz and is called resolution filter of R&S FSG. The filtered signal is then sampled by ADC at 81.6MHz sampling rate. The sampled IF signal is digitally down-converted to complex baseband and then lowpass filtered and resampled. The sampling rate can be chosen between 10KHz to 81.6MHz in step of 0.1Hz, and the choice of this affects the processing time and the maximum recording time. These samples are stored in the memory. R&S FSG has a special

memory of 4Mega samples for the I- and Q- data. The samples of the I- and Q- data are read out from the memory in the blocks of 512K each in ASCII or binary format.

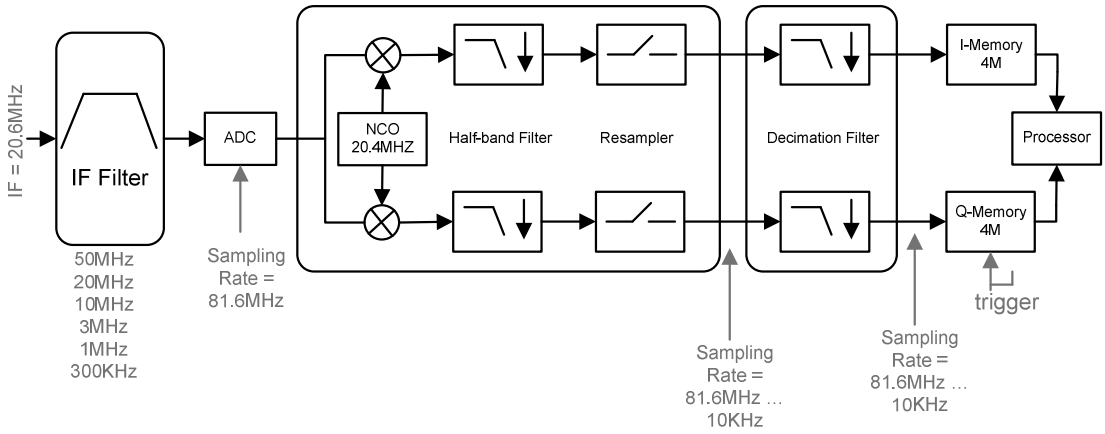

Figure 5.4: *I/Q subsystem from IF to baseband processor of R&S FSG [30].*

5.3 Measurement Results

Measurement results presented in this section demonstrate the performance of pre-distortion algorithms discussed in sections 3.5 and 3.6. The results are arranged in three different sections. First, front-end image rejection ratio without pre-distortion of MAX2023 chip is plotted for 1.5 GHz and 2.0 GHz RF frequency and based on the results, a suitable operating frequency for the measurements is determined. The second part assumes widely-linear least-square pre-distortion scheme and the measurement results are illustrated with constellation diagrams, image rejection ratio plots, and spectrum of the output RF signal. The third and final section presents the results of post-inverse estimation based pre-distortion scheme.

5.3.1. Front-End IRR without Calibration

The front-end IRR is estimated using a linearly modulated 16-QAM signal with 15MHz two-sided bandwidth. The signal has symbol rate of 12MHz, roll-off factor of 0.5, and oversampling factor is 6. The intention to choose such a large bandwidth is to estimate how the front-end of the chip behaves at different frequencies. The baseband signal is generated in the computer with Matlab and transferred to the memory of R&S AFQ, which samples the signal at 36MHz sampling frequency. The analog baseband signal outputted by R&S AFQ is modulated onto a RF carrier by MAX2023 modulator chip. A block of 100,000 samples, sampled at 72MHz rate, is measured by R&S FSG. The

measured data is resampled and nominally matched to the original signal. The reference and corrected measured data are used to estimate the imbalance filter $g_{1,T}(t)$ and $g_{2,T}(t)$ using (3.36). IRR curves with different imbalanced filter lengths, averaged over seven independent runs, are plotted in Figure 5.5 for 1.5 GHz (Figure 5.5-a) and for 2.0 GHz (Figure 5.5-b) centre frequency. The results suggest that the chip has frequency-selective IRR within the signal bandwidth varying between 32-37 dB at 1.5 GHz RF frequency and between 37-41 dB at 2.0 GHz RF frequency.

Estimated IRR is verified with another measurement example which considers a linearly modulated (16-QAM) low-IF signal with 7.5 MHz bandwidth and 4.5 MHz IF frequency. In order to verify the estimated IRRs of Figure 5.5, a low-IF signal is sent to the I/Q modulator and the spectrum of up-converted signal is shown in Figure 5.6 and Figure 5.7 for 1.5 GHz and 2.0 GHz RF frequency. Comparison of the measured spectra and IRR plot reveals that WLLS based algorithm is capable of correctly estimating the image signal attenuation.

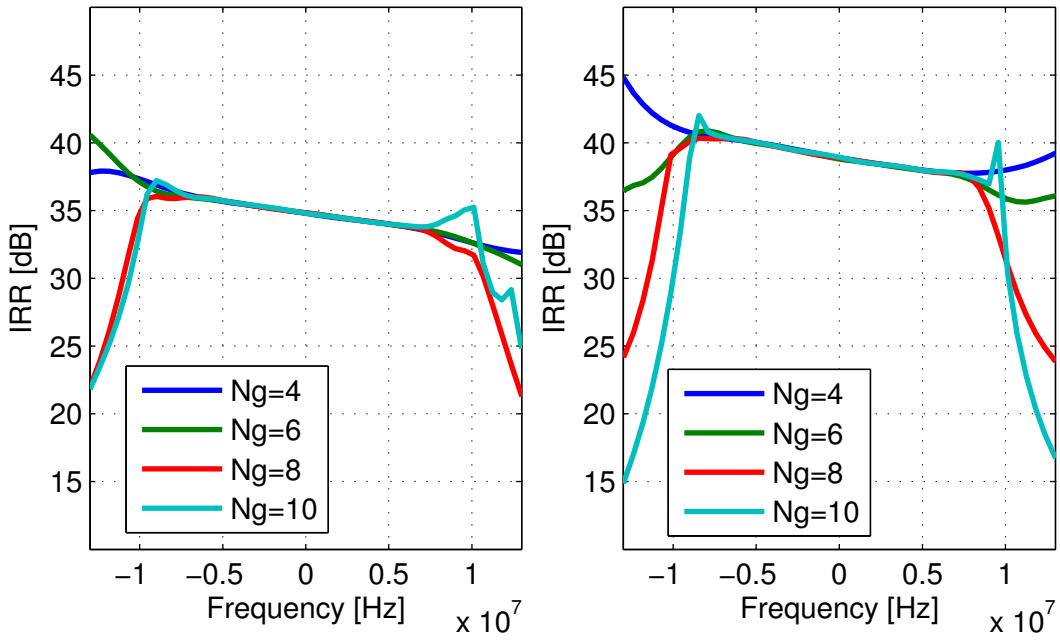

(a) *(b)*

Figure 5.5: *Comparison of averaged front-end IRR vs. frequency for different imbalance filter lengths. WLLS model fitting approach is used and the original signal has 15MHz overall bandwidth. (a) IRR vs. frequency curves for 1.5GHz centre frequency. (b) IRR vs. frequency curves for 2.0 GHz centre frequency.*

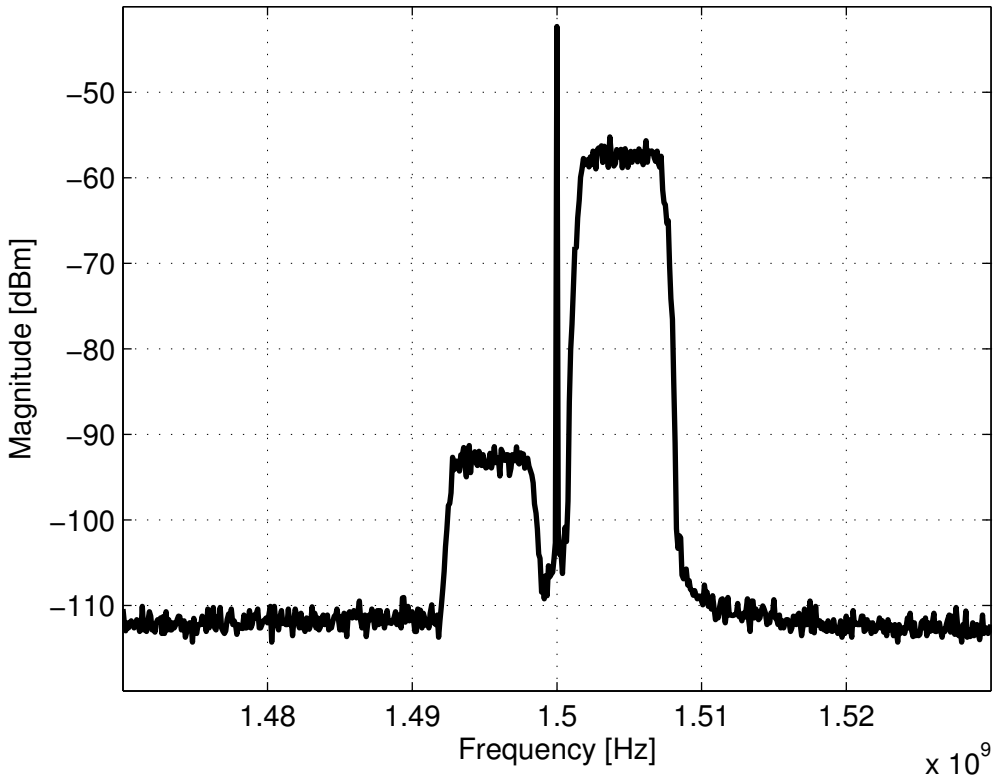

Figure 5.6: *Spectrum of measured signal at 1.5 GHz centre frequency. The original signal has 7.5 MHz bandwidth with 4.5 MHz IF frequency.*

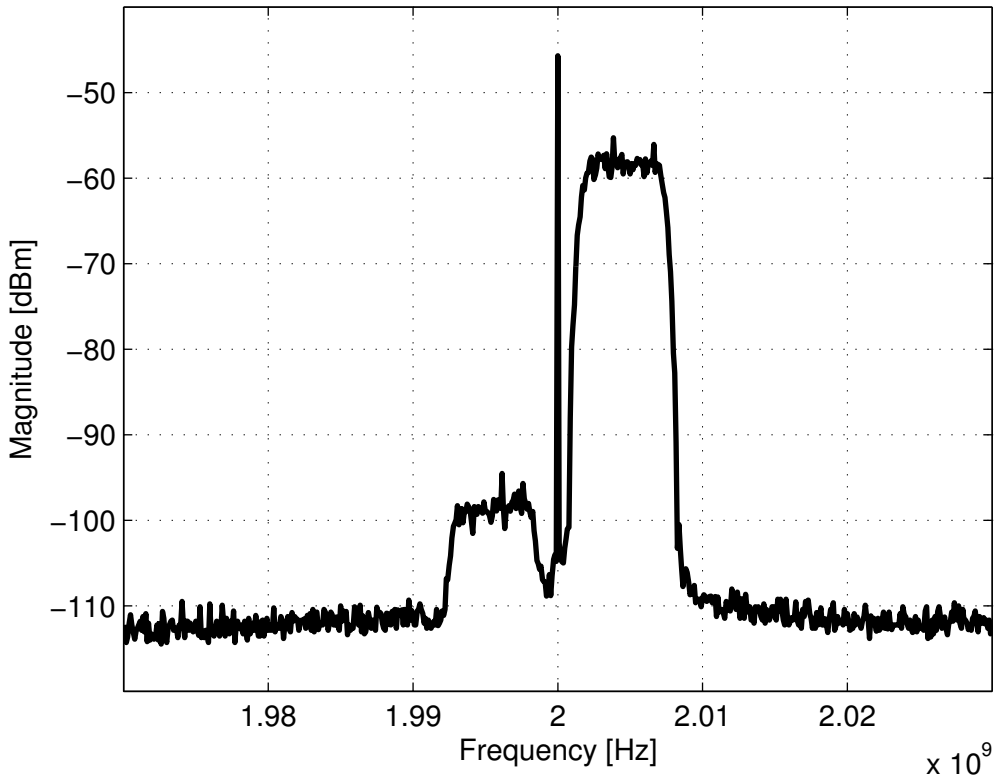

Figure 5.7: *Spectrum of measured signal at 2.0 GHz centre frequency. The original signal has 7.5 MHz bandwidth with 4.5 MHz IF frequency.*

5.3.2. Widely-Linear Least Squares Based Compensation Approach

In this section, the effectiveness of I/Q imbalance compensation algorithm designed in section 3.3.3 is evaluated using the proposed laboratory measurement setup. RF frequency of 1.5GHz is chosen for which the mirror-frequency attenuation of the front-end is frequency-selective varying between 32-37dB. Analog baseband signal is produced by the R&S AFQ. At startup, pre-distorter is switched off and a direct conversion modulator up-converts the baseband I/Q signal to RF frequency. In the feedback loop, the RF signal is down-converted to an IF frequency of 20.4 MHz by R&S FSG, which is then digitized and demodulated to the baseband using R&S FSG I/Q subsystem. The samples of baseband I- and Q- data are retrieved from the memory of R&S FSG. The measured data, after data conditioning, is used to estimate the pre-distortion filter parameters. After calculating the pre-distortion filter coefficients, the signal is pre-distorted and transmitted again through R&S AFQ.

The first measurement example corresponds to a linearly modulated 64-QAM signal with 15MHz waveform bandwidth. Symbol rate is 12MHz and roll-off factor is 0.25.

This baseband signal generated in the computer is sampled by R&S AFQ at a rate of 36MHz while R&S FSG samples the detected signal at 72MHz to down-convert it to baseband. The measured baseband data is resampled again to 36MHz and a set of 25,000 samples is compared with the reference data to estimate the calibration filter using widely-linear least-squares approach. The estimator filters length $g_{1,T}(t)$ and $g_{2,T}(t)$ is fixed to 3-taps, while the calibration performance is illustrated for pre-distortion filter lengths of 1, 2, and 3. The obtained mirror-frequency attenuation averaged over seven independent runs is plotted in

Figure 5.*8* as a function of frequency. In Figure 5.9-a, constellation diagram of signal corrupted with I/Q imbalance signal is depicted and Figure 5.9-b shows the compensated constellation diagram. For reference, the ideal constellation points are also shown in the figure and marked with "+" sign. As can be observed from

Figure 5.*8*, the clear improvement of more than 20dB in the front-end IRR can be obtained with proposed scheme as the filter length approaches its optimum value.

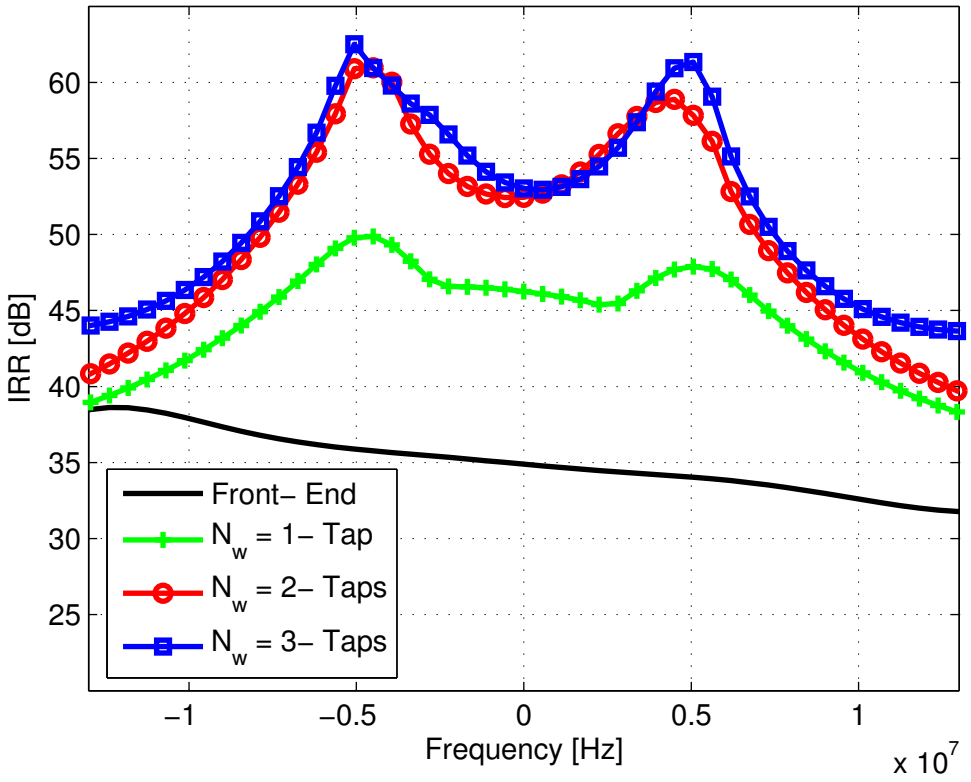

Figure 5.8: *Comparison of IRR vs. frequency curves for a direct conversion transmitter case with and without I/Q compensation. WLLS based I/Q compensator with different pre-distortion filter lengths is assumed. The signal has 15MHz bandwidth.*

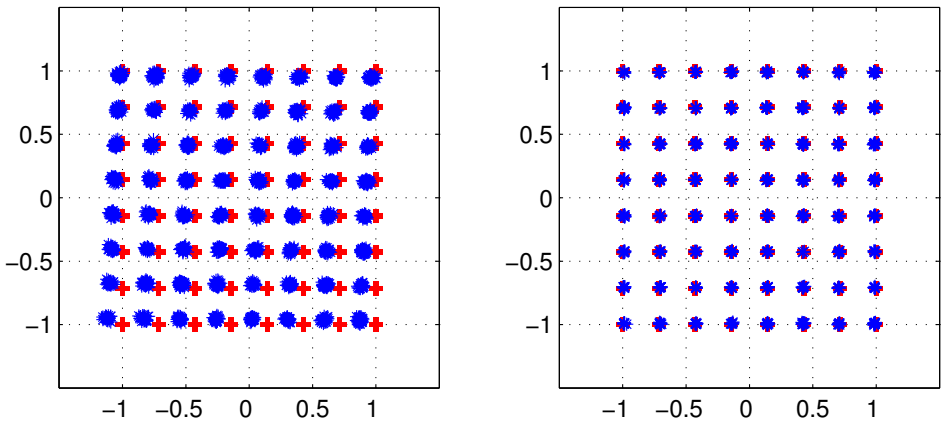

(a) *(b)*

Figure 5.9: *Constellation diagram of 64-QAM baseband signal before and after I/Q compensation. The I/Q compensator is constructed using WLLS technique. Ideal constellation points are marked as "+". (a) Without I/Q compensation (b) With a 3-taps pre-distortion filter.*

The next demonstration considers a low-IF signal with 7.5MHz bandwidth and 4.5MHz transmitter IF frequency. The calibration filter is the same used in last measurement example. The reason of this is to have a better spectral support for the estimator and also to make the system work independent of used waveform. Pre-distorted I/Q signal is transmitted through R&S AFQ and the spectrum of the pre-distorted RF signal captured from R&S FSG spectrum analyzer is shown in Figure 5.10. Again, the imbalanced filter length is fixed to 3-taps and IRR is plotted for calibration filter of length 1, 2, and 3. Estimated IRR is plotted in Figure 5.11. Based on Figure 5.11, the highest image attenuation is achieved in the region where mirror frequencies truly exist and the pre-distorter is able to improve the front-end IRR by 20-25dB, pushing the image frequencies close to the noise floor.

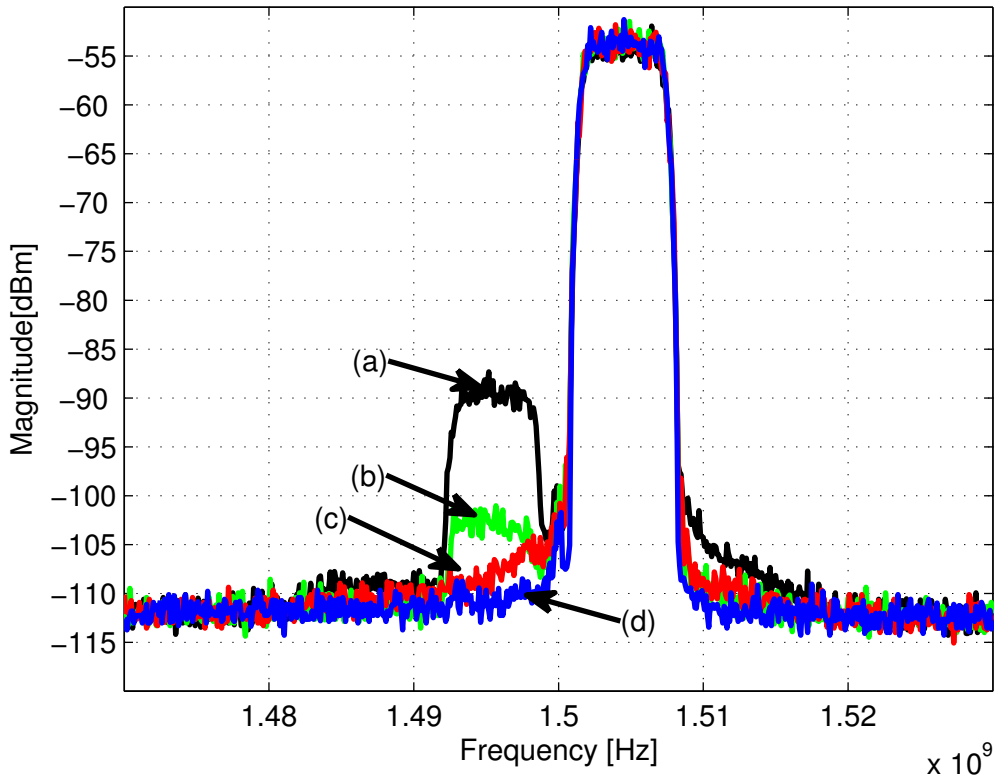

Figure 5.10: *Comparison of I/Q modulator output before and after I/Q imbalance compensation with different pre-distortion filter lengths. WLLS based compensation technique is considered. (a) Uncompensated signal. (b) With a 1-tap pre-distortion filter. (c) With a 2-taps pre-distortion filter. (d) With a 3-taps pre-distortion filter.*

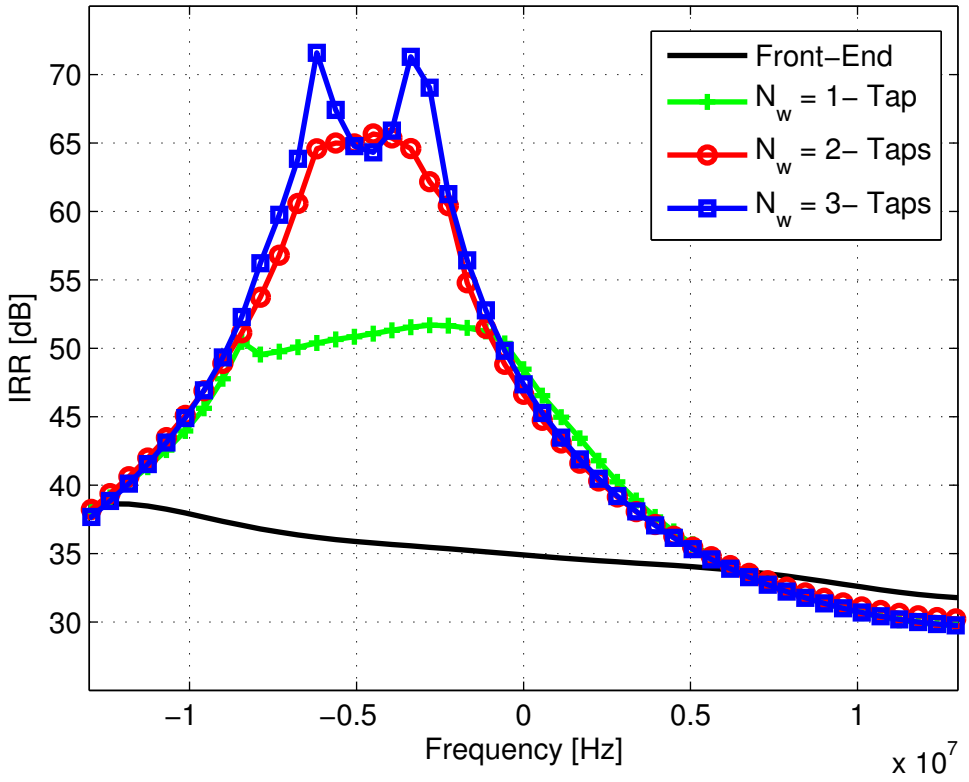

Figure 5.11: *Comparison of IRR vs. frequency curves for the low-IF transmitter case with and without I/Q compensation. WLLS based I/Q compensator with different pre-distortion filter lengths is assumed. The signal has 7.5MHz bandwidth and 4.5MHz IF frequency.*

The next situation examines the situation in which an OFDM signal is transmitted. The subcarrier spacing is 19.5 KHz and total number of subcarriers is 1024, out of which 768 are active. This corresponds to an overall bandwidth of 15 MHz, as shown in Figure 5.12. Same transmitter front-end is assumed with frequency-selective image attenuation and imbalanced filter length is fixed to 3-taps. Again, a block of 25,000 samples is used to estimate the compensation filter. Achieved image rejection ratio as a function of frequency is plotted in Figure 5.13 for different compensator filter lengths. Figure 5.14 shows the constellation plot before and after the compensation with 3-taps pre-distortion filter.

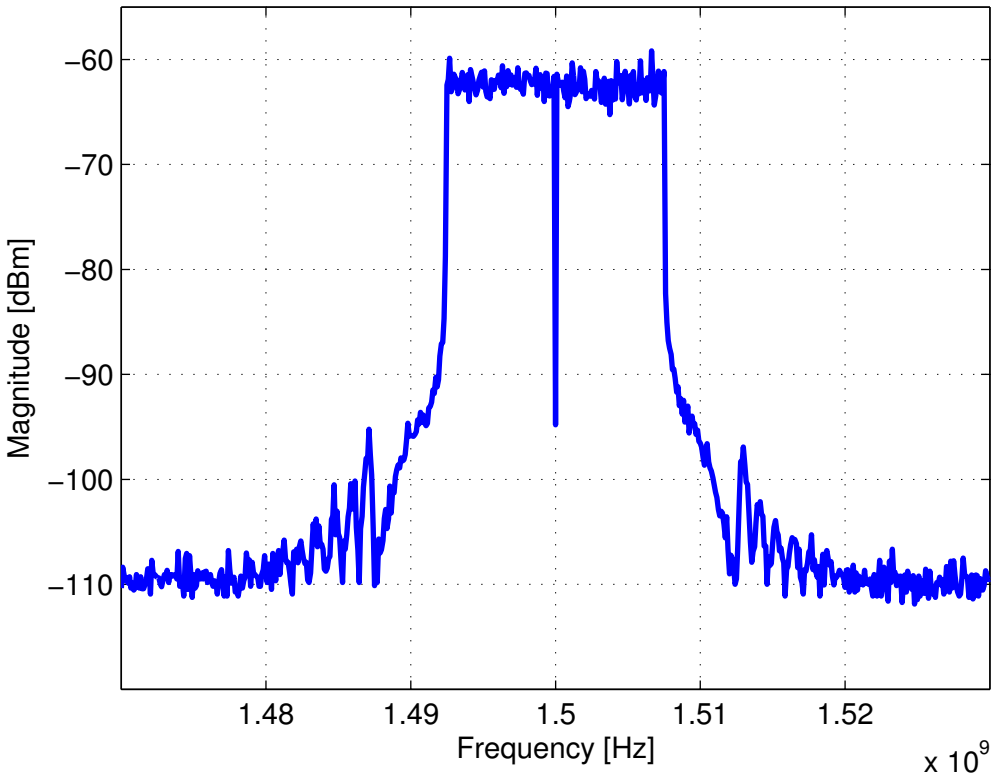

Figure 5.12: *The spectrum of an up-converted OFDM signal with 1.5GHz RF frequency. Total number of subcarriers are 1024 and 768 are active. Subcarrier spacing is 19.5 KHz.*

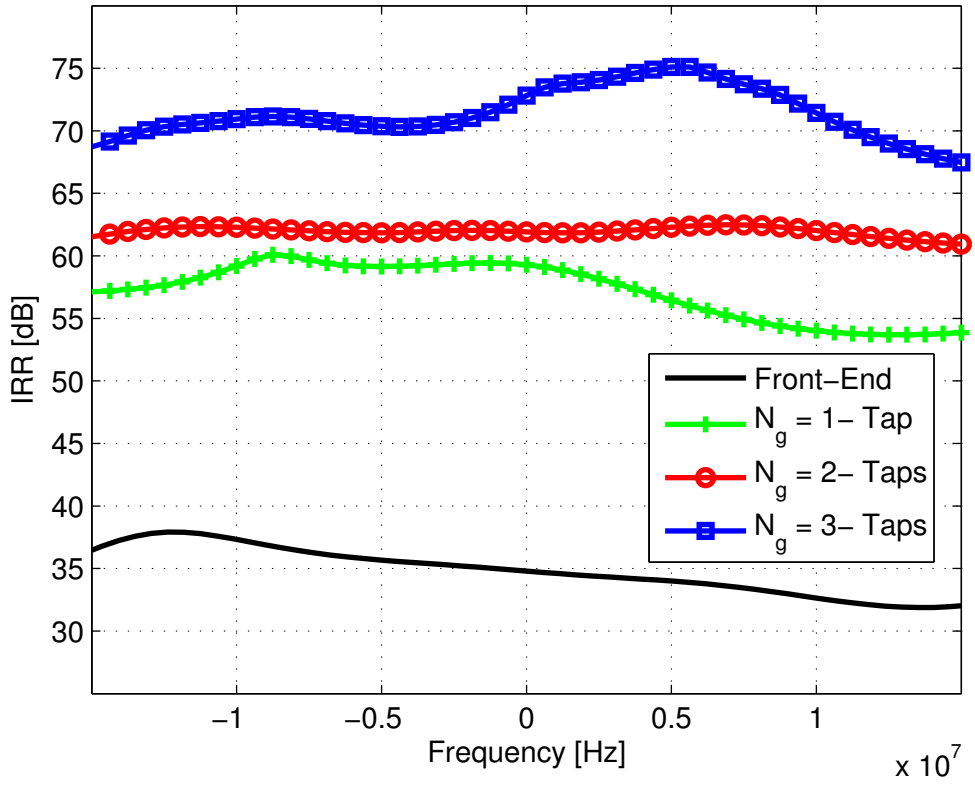

Figure 5.13: *Comparison of IRR vs. frequency curves for the OFDM transmitter case with and without I/Q compensation. WLLS based I/Q compensator with different pre-distortion filter lengths is assumed. The signal has 15 MHz bandwidth.*

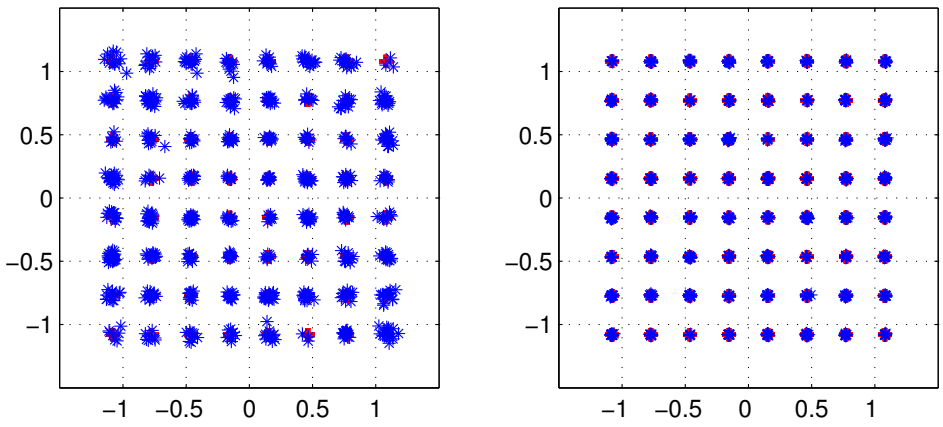

(a) *(b)*

Figure 5.14: *Constellation diagram of OFDM signal with 64-QAM baseband modulation before and after I/Q compensation. The I/Q compensator is constructed using WLLS technique. (a) Without I/Q compensation. (b) With a 3-taps pre-distortion filter.*

5.3.3. Post-Inverse Estimation Approach

Here, the efficiency of algorithms based on post-inverse of the I/Q channel is evaluated. The measurement examples consider the same low-IF and OFDM signals discussed in the previous section. The figure of merit in the following measurements will be constellation diagram or spectrum plots. Also, to improve the estimation of compensation filters, a low-level Gaussian noise has been added to the original signal as stated in section 3.6. In all the measurements, a block of 30, 000 samples is measured from R&S FSG and matched nominally with the input signal. After data conditioning, I/Q compensator is constructed by the approach discussed in section 3.6 and the I- and Q- data of the original signal are pre-distorted. The output after pre-distortion is shown in Figure 5.15 for low-IF signal with 7.5MHz bandwidth. In Figure 5.16, constellation diagram before and after pre-distortion is depicted for OFDM signal.

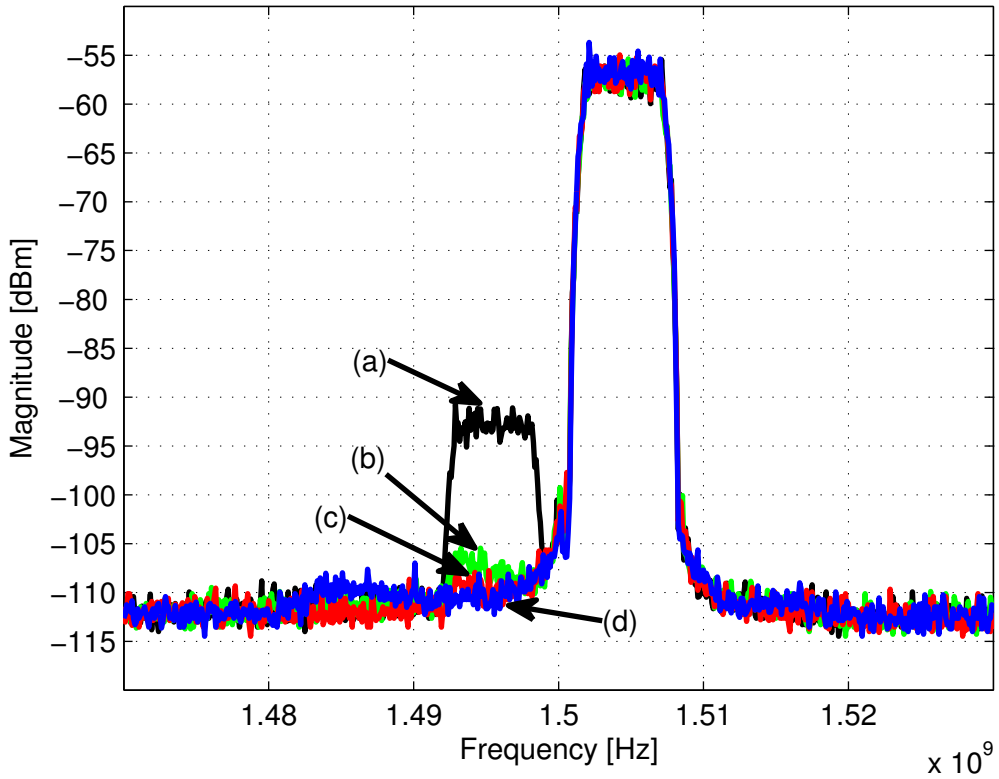

Figure 5.15: *Comparison of I/Q modulator output before and after I/Q imbalance compensation with different pre-distortion filter lengths. Post-inverse estimation based compensation technique is considered. (a) Uncompensated signal. (b) With a 1-tap pre-distortion filter. (c) With a 2-taps pre-distortion filter. (d) With a 3-taps pre-distortion filter.*

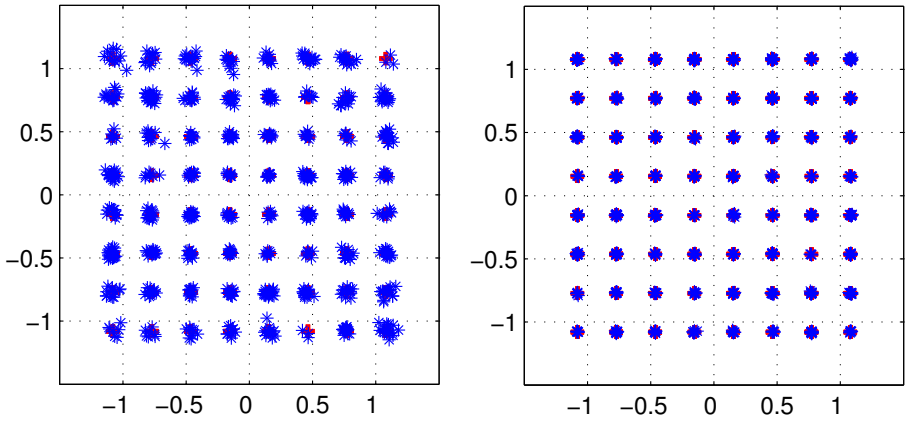

(a) *(b)*

Figure 5.16: *Constellation diagram of OFDM signal with 64-QAM baseband modulation before and after I/Q compensation. The I/Q compensator is constructed using post-inverse estimation technique. (a) Without I/Q compensation. (b) With a 3-taps pre-distortion filter.*

5.4 Comparison with Simulation Results

A comparison of computer simulation results and obtained measurement results is shown in Figure 5.17. For the low-IF type signals, achieved IRR value with measurements is slightly smaller than the actual simulated IRR, in contrast to the baseband type signals where the difference of IRR values between the simulation and measurement values amounts to approximately 15-20dB. The large difference in the latter case could be due to the noise and other source of non-idealities present in the practical systems which make the estimation of calibration filter parameters difficult. However, it is important to note that IRR requirements are not stringent for direct conversion transmitters and an IRR in the order of 50-60 dB offered by the algorithms is stated feasible in literature.

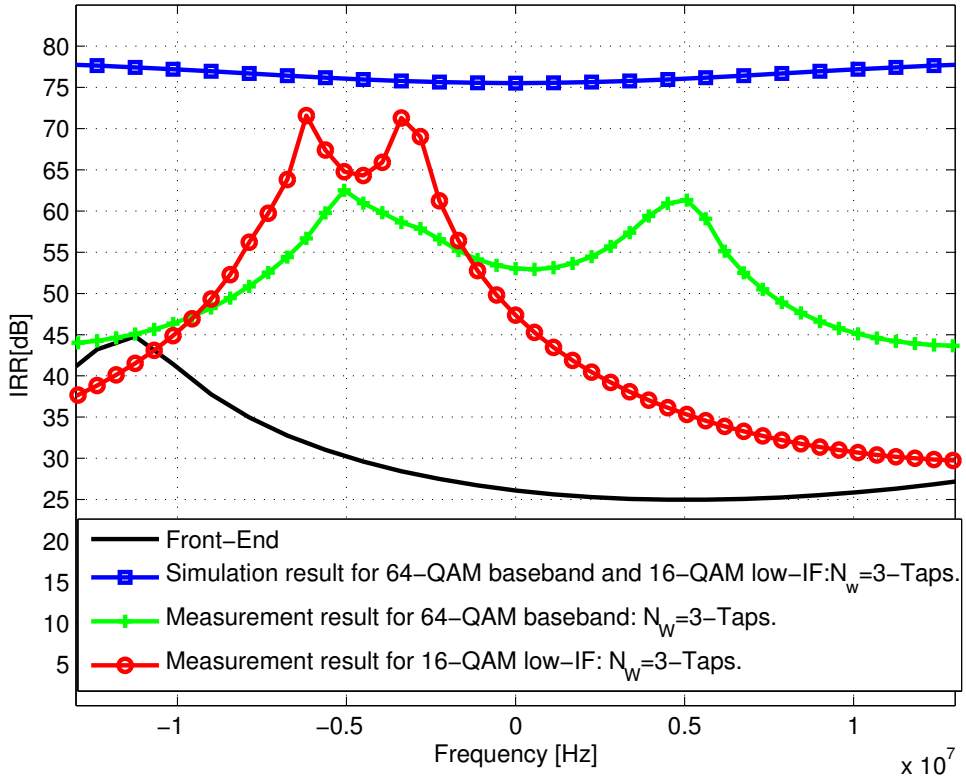

Figure 5.17: *Comparison of IRR vs. frequency curves obtained with simulations and measurements for different signal models.*

5.5 Discussion

A laboratory measurement setup is presented in this chapter to analyze the effects of analog I/Q impairments in the direct conversion transmitters and to evaluate the calibration performance of the algorithms discussed in Chapter 3. The measurement setup is made up of a direct conversion modulator, signal generators, and a spectrum and signal analyzer. The mirror-frequency attenuation of the direct conversion modulator is frequency-dependent and is in the order of 32-37dB without calibration. Two different pre-distortion techniques, namely, widely-linear least-square technique and post-inverse estimation based techniques, , are implemented in the computer and tested with different signal models. In all the measurements, a block of 30000 samples is captured from R&S FSG. This measured data is further processed in the computer to determine the feedback loop gain, phase, delay, DC offset, and frequency offset. Frequency synchronization is achieved by using a single reference oscillator of R&S FSG spectrum analyzer to generate both up- and downconversion LO signals. LO signal leakage manifests itself to DC offset in the measured signal, which is compensated by

subtracting the mean value of the data from the measured signal. After the measured data conditioning, pre-distortion filter is computed by the two approaches. The spectrum of the pre-distorted signal and estimated IRR plots indicates that both approaches are able to fully suppress the image signals. A pre-distortion filter of 3-taps pushes the image signal below the noise floor and achieves an image signal attenuation of more than 60 dB. However, some residue image is left with 1-tap and 2-taps pre-distortion filters. The I/Q compensator consist of one complex filter in the case of WLLS technique, whereas, four real filters are utilized in the post-inverse estimation based technique. Therefore, WLLS technique is computationally less complex than the post-inverse estimation technique.

Chapter 6

Conclusions

There is a strong drift towards devices that support existing as well as emerging radio standards. Classical super-heterodyne architecture has been used in most of the earlier wireless transceivers, but the inherent problems associated with this architecture like high power consumption and difficulty to integrate make it unfavorable for future wireless applications. Alternatively, architectures such as direct conversion and low-IF are becoming increasingly popular as they offer a better choice of simplified front-end by eliminating many off-chip components used in super-heterodyne architecture. These architectures employ the complex mixing principle for up- and downconversion and relieve high quality RF filtering requirements of a transceiver.

Radio transceivers based on complex mixing suffer from I- and Q- mismatches. This is because the characteristics of the components used in the quadrature branches can only be matched to a certain degree and there is always some imbalance in practical implementations. With current analog electronics, a typical quadrature modulator/demodulator has 2-3^{o} phase error and 1-2% amplitude error resulting in image suppression of only 30-40 dB (Figure 3.1), which is insufficient for future multi-channel, multi-user radio terminals.

The overall topic of this thesis was to investigate the performance of pre-distortion based algorithms for transmitter I/Q mismatch calibration. For this purpose, two compensation algorithms utilizing the feedback signal were considered. First, the general signal analysis of an imbalanced LO signal was carried out and image rejection ratio was defined in terms of oscillator gain and phase. The evaluation of frequency dependent I/Q imbalance model shows that the baseband equivalent of imbalanced RF signal is summation of baseband signal $x(t)$ and its image $x^{*}(t)$, filtered by the

imbalance filters $g_{1,T}(t)$ and $g_{2,T}(t)$, respectively. The imbalance filters model the gain imbalance, phase imbalance, and DACs frequency response. The analytic solution of the optimum pre-distortion filter yield the ratio of the discrete Fourier transform of the imbalance filters, $-G_{2,T}(f)$ and $G_{1,T}(f)$. Two techniques for estimating the pre-distortion filter were discussed next and compensator structures were derived based on the algorithms. The first scheme was based on the widely-linear least-squares model fitting of the measured and original data to estimate calibration filter parameters. In the second approach, I/Q imbalance was modeled as the cross-coupled real filters in the I- and Q- branch whose inverse was determined to mitigate I/Q imbalance. The efficiency of the compensation schemes was evaluated with computer simulations and the reported results demonstrate the good calibration performance. A prototype structure consisting of laboratory instruments was presented and extensive measurements with different waveform formats were carried out to prove the practical value of algorithms. Based on the measurement results it was shown that compensation algorithms have very excellent performance and provide significant improvement in front-end IRR. In general, IRR's in the order of 50-80dB were demonstrated with both calibration techniques using measured laboratory radio signals.

References

[1] B. Razavi, *RF Microelectronics,* Prentice-Hall, 1998.

[2] A. Luzzatto and G. G. Shirazi, *Wireless Transceiver Design,* John Wiley and Sons, 2007.

[3] A. Katz, "Linearization, Reducing Distortion in Power Amplifiers," *IEEE Microwave Mag.* Vol. 2, pp. 37-49, Dec. 2001.

[4] P. B. Kenington, "Linearized Transmitters: An Enabling Technology for Software Defined Radio," *IEEE Communication Mag.* Vol. 40, pp. 156-162, Feb. 2002.

[5] P. B. Kenington, *High Linearity RF Amplifier Design,* Norwood, MA: Artech House, 2000.

[6] T. Turlington, *Behavioral Modeling of Nonlinear RF and Microwave Devices,* Artech, 2000.

[7] J. Mahattanakul, "The Effect of I/Q Imbalance and Complex Filter Component Mismatch in Low-IF Receivers," *IEEE Trans. On Circuits and Systems,* Vol. 53, No. 2, Feb. 2006.

[8] L. Ding, *Digital Predistortion of Power Amplifiers for Wireless Applications,* Phd. Thesis, Georgia Institute of Technology, USA, March 2004.

[9] M. Valkama, *Advanced DSP for I/Q Imbalance Compensation in Digital Receivers,* M.Sc. Thesis, Tampere University of Technology, Finland, Jan. 2000.

[10] F. Horlin, A. Bourdoux, *Digital Compensation of Analog Front-End,* John Wiley and Sons, 2008.

[11] G. Heuber and R. B. Staszewski, *Multi-Mode/Multi-Band RF Transceivers for Wireless Communications,* John Wiley and Sons, 2009.

[12] M. Golio, *RF and Microwave Handbook,* CRC Press, 2001.

[13] J. H. Reed, *Software Radio,* Prentice Hall, 2002.

[14] T. M. Windisch, *Estimation and Compensation of I/Q Imbalance in Broadband Communications Receivers,* Phd. Thesis, Dresden University of Technology, Germany, March 2001.

[15] A. B. Carlson, *Communication Systems,* 3rd Ed., New York: McGraw Hill, 1986.

[16] L. W. Couch, *Digital and Analog Communication Systems,* 7th Ed., Prentice Hall, 2007.

[17] Q. Gu, *RF System Design of Transceivers for Wireless Communications,* Springer, 2005.

[18] E. A. Lee and D. G. Messerschmitt, *Digital Communications,* Boston, MA: Kluwer Academic Publisher, 1988.

[19] S. Mirabbasi and K. Martin, "Classical and Modern Receiver Architectures," *IEEE Communications Mag.*, Vol. 38, pp. 132-139, Nov. 2000.

[20] M. Valkama, *Advanced I/Q Signal Processing for Wideband Receivers: Models and Algorithms,* Phd. Thesis, Tampere University of Technology, Finland, Nov. 2001.

[21] M. Windisch and G. Fettweis, "Adaptive I/Q Imbalance Compensation in Low-IF Transmitter Architectures," *IEEE Vehicular Tech. Conference,* Vol. 3, pp. 2096-2100, Sept. 2004.

[22] S. J. Chen and Y. H. Hsieh, *IQ Calibration Techniques for CMOS Radio Transceivers,* Springer 2006.

[23] L. Anttila, M. Valkama, and M. Renfors, "Frequency-Selective I/Q Mismatch Calibration for Wideband Direct Conversion Transmitters," *IEEE Trans. on Circuits and Systems,* Vol. 55, pp. 359-363, April 2008.

[24] L. Ding, Z. Ma, D. R. Morgan, M. Zierdt, and G. T. Zhou, "Compensation of Frequency Dependent Gain/Phase Imbalance in Predistortion Linearization Systems," *IEEE Trans. on Circuits and Systems,* Vol. 55, pp. 390-397, Feb. 2008.

[25] B. Picinbono and P. Chevalier, "Widely Linear Estimation with Complex Data," *IEEE Trans. on Signal Processing,* Vol. 43, pp. 2030-2033, Aug. 1995.

[26] U. Mengali and A. N. D. Andrea, *Synchronization Techniques for Digital Receivers,* Plenum Press, 1997.

[27] S. Haykin, *Adaptive Filter Theory,* 4th Ed., Upper Saddle River, NJ: Prentice Hall, 2002.

[28] L. YU and W. M. Snelgrove, "A Novel Adaptive Mismatch Cancellation System for Quadrature IF Radio Receivers," *IEEE Trans. on Circuits and Systems-II, Analog Digital Signal Processing,* Vol. 49, No. 6, pp. 789-801, June 1999.

[29] M. Valkama, M. Renfors, and V. Koivunen, "Advanced Methods for I/Q Imbalance Compensation in Communication Receivers," *IEEE Trans. on Signal Processing,* Vol. 49, pp. 2335-2344, Oct. 2001.

[30] Rohde&Schwarz. [Online] Available: http://www2.rohde-schwarz.com/

[31] Maxim ICs. [Online] Available: http://www.maxim-ic.com/

[32] G. Fettweis, M Löhning, D. Petrovic, M. Windisch, P. Zillman, and W. Rave, "Dirty RF: A New Paradigm," *In Proc. 16th IEEE International Symposium on Personal, Indoor, and Mobile Radio Communication,* (PIMRC'05), Berlin, Germany.

[33] W. Tuttlebee, *Software Defined Radio: Enabling Technologies,* Wiley, 2002.

[34] J. C. Rudell, J. J. Qu, R. S. Narayabaswani, G. Chien, K. A. Weldon, L. Lin, K.-C. Tsai, L. Tee, K. Khoo, D. Au, T. Robinson, D. Gerna, M. Otsuka, and P. R. Gray, "Recent Developments in High Integration Multi-Standard CMOS Transceivers for Personal Communication Systems," *In Proc. IEEE Intl. Symposium on Low Power Electronics and Design,* Monterey, CA, USA, pp. 149-154, Aug. 1998.

[35] A. A. Abidi, "Direct conversion radio transceivers for digital communications," *IEEE J. Solid-State Circuits*, vol. 30, pp. 1399-1410, Dec. 1995.

[36] A. A. Abidi, "CMOS wireless transceiver: The new wave," *IEEE Commun. Mag.*, Vol. 37, pp. 119-124, Aug. 1999.

[37] A. A. Abidi, "Low-power radio-frequency ICs for portable communications," in L. E. Larson, Ed., *RF and Microwave Circuit Design for Wireless Communications*. Norwood, MA: Artech House, 1996, pp. 43-98.

[38] E. Cetin, I. Kale, and R. C. S. Morling, "Joint Compensation of IQ-Imbalance and Carrier Phase Synchronization Errors in Communication Receivers," *IEEE International Symposium on Circuits and Systems,* Kobe, Japan, May 2005.

[39] E. Cetin, I. Kale, and R. C. S. Morling, "Adaptive Compensation of Analog Front-End I/Q Mismatches in Digital Receivers," *IEEE International Symposium on Circuits and Systems,* Sydney, Australia, May 2001.

[40] E. Cetin, I. Kale, and R. C. S. Morling, "Living and Dealing with RF Impairments in Communication Transceivers," *IEEE International Symposium on Circuits and Systems,* New Orleans, Louisiana, USA, May 2007.

[41] Agilent Technologies. [Online] Available: www.agilent.com

[42] T. J. Rouphael, *RF and Digital Signal Processing for Software Defined Radio,* Elsevier, 2008.

[43] C. Chien, *Digital Radio Systems on a Chip,* Kluwer Academic Publisher Group, 2000.

[44] A. Swaminathan, M. Snelgrove, S. Jantzi, and S. Bazarjanil, "A Monolithic Complex Sigma-Delta Modulator for Digital Radio," *in Proc. 1996 IEEE-CAS Region 8 Workshop on Analog and Mixed IC Design,* pp.83, Pavia, Italy, Sept. 1996.

[45] S. A. Jantzi, K. W. Martin, "The Effect of Mismatch in Complex Bandpass $\Delta\Sigma$ Modulators," in Proc. ISCAS 1996, pp. 227-230, Atlanta, GA, USA, May 1996.

[46] R. Marchesani, "Digital Precompensation of Imperfections in Quadrature Modulators," *IEEE Trans. Comm.,* Vol. 8, PP. 552-556, April 2000.

[47] S. A. Leyonhjelm and M. Faulkner, " The Effect of Reconstruction Filters on Direct Upconversion in a Multichannel Environment," *IEEE Trans. Veh. Technol.,* Vol. 44, PP. 95-102, Feb. 1995.

[48] J. Tuthill and A. Cantoni, "Efficient Compensation for Frequency-Dependent Errors in Analog Reconstruction Filters Used in IQ Modulators," *IEEE Trans. Commun. ,*Vol. 53, PP. 489-496, March 2005.

[49] J. K. Cavers, and M. W. Liao, "Adaptive Compensation for Imbalance and Offset Losses in Direct Conversion Transceivers," *IEEE Trans. Veh. Tecnol.,* Vol. 42, No. 4, PP. 581-588, Nov. 1993.

[50] J. K. Cavers, "The Effect of Quadrature Modulator and Demodulator Errors on Adaptive Digital Predistorter for Amplifier Linearization," *IEEE Trans. Veh. Technol.,* Vol. 46, No. 2, PP. 456-466, May 1997.

[51] J. Mahattanakul, "The Effect of I/Q Imbalance and Complex Filter Component Mismatch in Low-IF Receivers," *IEEE Trans. Circuits Syst. I, Reg. Papers,* Vol. 53, No. 2, PP. 247-253, Feb. 2006.

[52] M. Faulkner, T. Mattsson, and Y. Yates, "Automatic Adjustment of Quadrature Modulators," *Electron. Lett.,* Vol.27, PP. 214-216, Jan. 1991.

[53] GSM Association. [Online] Available: http://www.gsmworld.com